Article

SOURCE DATA | TRANSPARENT PROCESS

THE EMBO JOURNAL

Avidity-driven polarity establishment via multivalent lipid–GTPase module interactions

Julien Meca[1,†], Aurélie Massoni-Laporte[1,†], Denis Martinez[2], Elodie Sartorel[1], Antoine Loquet[2], Birgit Habenstein[2] & Derek McCusker[1,*]

Abstract

While Rho GTPases are indispensible regulators of cellular polarity, the mechanisms underlying their anisotropic activation at membranes have been elusive. Using the budding yeast Cdc42 GTPase module, which includes a guanine nucleotide exchange factor (GEF) Cdc24 and the scaffold Bem1, we find that avidity generated via multivalent anionic lipid interactions is a critical mechanistic constituent of polarity establishment. We identify basic cluster (BC) motifs in Bem1 that drive the interaction of the scaffold–GEF complex with anionic lipids at the cell pole. This interaction appears to influence lipid acyl chain ordering, thus regulating membrane rigidity and feedback between Cdc42 and the membrane environment. Sequential mutation of the Bem1 BC motifs, PX domain, and the PH domain of Cdc24 lead to a progressive loss of cellular polarity stemming from defective Cdc42 nanoclustering on the plasma membrane and perturbed signaling. Our work demonstrates the importance of avidity via multivalent anionic lipid interactions in the spatial control of GTPase activation.

Keywords cell polarity; lipids; nanoclustering; Rho GTPase; super-resolution imaging

Subject Categories Cell Adhesion, Polarity & Cytoskeleton; Membrane & Intracellular Transport

DOI 10.15252/embj.201899652 | Received 16 April 2018 | Revised 26 October 2018 | Accepted 2 November 2018 | Published online 17 December 2018

The EMBO Journal (2019) 38: e99652

Introduction

Cellular polarity, the anisotropic organization of cellular constituents, is essential for basic cellular functions including migration, division, and polarized growth (Drubin & Nelson, 1996). In diverse eukaryotes, cellular polarity is regulated by GTPases of the Rho family, including Cdc42 (Johnson & Pringle, 1990; Stowers *et al*, 1995; Gotta *et al*, 2001; Kay & Hunter, 2001; Atwood *et al*, 2007). The temporal and spatial control of Cdc42 activity on the plasma membrane ensures the anisotropic activation of the protein and thus its function as an essential regulator of cellular polarity.

Cdc42 is prenylated at its C-terminus via the covalent addition of an S-geranylgeranyl group and methylesterification of a cysteine residue (Ghomashchi *et al*, 1995). These modifications, together with juxtaposed polybasic residues, facilitate the high affinity binding of the GTPase to membrane (Finegold *et al*, 1991; Kozminski *et al*, 2000). While lipid modification ensures the membrane association of the protein, it is not sufficient to account for its anisotropic localization (Richman *et al*, 2002, 2004). Rather, the enrichment of Cdc42 at the cell pole is thought to reflect the local activation of the GTPase by its GEF Cdc24 and stabilization of the GEF-Cdc42 complex involving the scaffold Bem1 (Butty *et al*, 2002; Toenjes *et al*, 2004).

How then, are Bem1 and Cdc24 recruited to the plasma membrane to locally activate Cdc42? Both are peripheral membrane proteins containing a pleckstrin homology (PH) domain in the case of Cdc24 and a Phox (PX) domain in Bem1. However, the PH domain in Cdc24 displays no detectable phosphoinositide specificity *in vitro*, nor is fusion of the PH domain to GFP sufficient for membrane targeting (Yu *et al*, 2004). These features reflect the low affinity of the Cdc24 PH domain for phosphoinositides (PI; $K_d > 20$ μM for PI4,5P2, for example; Yu *et al*, 2004). The PX domain of Bem1 binds PI3P, PI4P, and phosphatidylserine (PS) *in vitro*. While the affinity of the Bem1 PX domain for PI3P is low ($K_d > 100$ μM), its interaction with PS and PI4P was observed to be stronger (Yu & Lemmon, 2001; Stahelin *et al*, 2007). However, neutralization of a critical arginine required for electrostatic interactions with anionic lipids within the Bem1 PX domain did not disrupt Bem1 localization unless additional pathways that guide Cdc42 activation were also blocked (Irazoqui *et al*, 2003). The mechanism accounting for the site-specific recruitment of these critical Cdc42 regulators to the plasma membrane therefore represents a key unanswered question.

At the plasma membrane of diverse eukaryotes, anionic lipids including PS contribute to the net negative charge of the membrane and the recruitment of peripheral membrane proteins (Yeung *et al*, 2008; Haupt & Minc, 2017). Moreover, the localization of a PS reporter is anisotropic with respect to both the lateral plane of the

1 CNRS, UMR 5095, European Institute of Chemistry and Biology, University of Bordeaux, Pessac, France
2 CNRS, UMR 5248, European Institute of Chemistry and Biology, University of Bordeaux, Pessac, France
*Corresponding author. Tel: +33 5400 03021; E-mail: mccusker@iecb.u-bordeaux.fr
†These authors contributed equally to this work

plasma membrane and the inner leaflet of the membrane (Haupt & Minc, 2017). PS has been shown to play an important role in the anisotropic localization of Cdc42 and Bem1 in *Saccharomyces cerevisiae* (Fairn *et al*, 2011; Das *et al*, 2012). Work from our laboratory indicates that PS is required for the spatial organization of Cdc42 in nanoclusters on the plasma membrane, whose size correlates with Cdc42 activity. The addition of PS to wild-type cells results in larger Cdc42 nanoclusters at the cell pole in a Bem1-dependent manner (Sartorel *et al*, 2018). PS is emerging as a key regulator of nanoclustering in diverse signaling pathways, including Ras signaling (Raghupathy *et al*, 2015; Zhou *et al*, 2015, 2017). Defining how Cdc42 activators interact with anionic lipids including PS would therefore address one of the most upstream events during polarity establishment and may provide insight into more general features of Ras-family signaling that are conserved among eukaryotes.

Here, using complementary quantitative *in vivo* imaging and reconstitution experiments, we identify a mechanism through which the Cdc42 regulators are recruited to anionic lipids. The interaction of Bem1 with PS and PI4P influences lipid acyl chain fluidity depending on the membrane environment. The affinity of Bem1 for anionic lipids is also sufficient to target the associated GEF to this membrane environment, while robust membrane targeting of the GEF–scaffold complex involves multivalent protein–lipid interactions that promote Cdc42 nanoclustering, signaling, and cell polarity.

Results

Plasma membrane phosphoinositides and PS are essential for the polarized targeting of Cdc42 regulators *in vivo*

The sole PS synthase *CHO1* is not an essential gene in budding yeast, whereas the anisotropic localization of Cdc42 is essential, suggesting that other lipids may compensate for the lack of PS in *cho1*Δ cells to promote Cdc42 polarization. Phosphoinositides such as PI4P and PI(4,5)P2 play critical signaling roles at the plasma membrane and are therefore attractive candidates (Schink *et al*, 2016). Recent work uncovered a mechanism of PS transport from the ER to the plasma membrane involving the counter transport of PI4P in the opposite direction (Chung *et al*, 2015; Moser von Filseck *et al*, 2015). Consistently, plasma membrane PI4P levels have been reported to be elevated in *cho1*Δ cells, prompting us to examine whether this PI4P pool could account for the residual Cdc42 localization in the *cho1*Δ mutant (Zhong *et al*, 2012).

First, we examined the localization of Bem1-GFP in *cho1*Δ cells and confirmed that the percentage of cells displaying polarized Bem1-GFP was reduced compared to a wild-type (WT) control population (26% cells with polarized Bem1-GFP in *cho1*Δ, 71% in WT; Fig 1A and B; Fairn *et al*, 2011). In addition, the fluorescence intensity of Bem1-GFP was also reduced at the pole of those *cho1*Δ cells that displayed polarized Bem1-GFP (Fig EV1A). Next, we observed an approximately 2.5-fold increase in the intensity of a PI4P probe at the plasma membrane by quantitative imaging in *cho1*Δ cells (Fig 1C and D). Analysis of the fluorescence ratio between the cell pole and mother cell indicated enrichment of the probe at the pole (Fig 1E). This is consistent with previous reports of increased global PI levels and a specific increase in PI4P in *cho1*Δ cells (Fairn *et al*, 2011; Zhong *et al*, 2012). The increase was not due to obvious differences in the expression levels of the fluorescent probe, as both PS and PI4P probes were expressed similarly in WT and *cho1*Δ mutant cells (Fig EV1B and C). Bem1-GFP localization appeared qualitatively unperturbed in *osh6*Δ *osh7*Δ mutants, which have been implicated in PS-PI4P counter transport (Fig EV1D), prompting us to focus on whether direct PS and PI4P ablation affected the localization of Bem1 (Moser von Filseck *et al*, 2015). We appended an auxin-inducible degradation signal to the plasma membrane PI-4-kinase Stt4 in the *cho1*Δ mutant (Nishimura *et al*, 2009; Morawska & Ulrich, 2013). As expected, the double mutant was sensitive to the presence of auxin and choline in the media (Fig EV1E and F). Quantitative imaging indicated reduced plasma membrane levels of a PI4P probe upon auxin treatment (Fig EV1G and H). In addition, the levels of 9XMyc-AID-stt4 were reduced after

Figure 1. Plasma membrane phosphoinositides and PS are essential for the polarized targeting of Cdc42 regulators *in vivo*.

A Representative images of Bem1-GFP and the PS marker LactC2-GFP in wild-type and *cho1*Δ cells. Images show average intensity projections of deconvolved *z*-stacks. Black and white pixels were inverted to improve contrast for display.

B Frequency of cells displaying polarized Bem1-GFP signal in wild-type and *cho1*Δ cells. Values are means ± SD, $n > 100$ cells in each of three independent experiments. Paired Student's *t*-tests were performed.

C Imaging of the PI4P probe GFP-2xPH^{Osh2} in wild-type and *cho1*Δ cells. Images show average intensity projections of deconvolved *z*-stacks in which black and white pixels were inverted.

D Scatter dot plot showing PI4P levels at the plasma membrane (see experimental procedure for details of the quantification) in wild-type and *cho1*Δ cells. Values are means ± SD, $n > 100$ cells, observed over three experiments. Mann–Whitney tests were performed.

E Ratio of PI4P average fluorescence intensity in the bud versus mother cell in the *cho1*Δ mutant. Values are means ± SD, $n > 100$ cells, observed over three experiments. A value > 1 indicates enrichment of the fluorescence in the bud.

F Images of Bem1-GFP in *cho1*Δ *9xMyc-AID-stt4* cells after 30 min treatment with or without 0.5 mM auxin. Images are average intensity projections of deconvolved *z*-stacks.

G Frequency of cells with polarized Bem1-GFP signal or Bem1-GFP in puncta in *cho1*Δ *9xMyc-AID-stt4* cells treated with or without auxin as shown in (F). Values are means ± SD, $n > 100$ cells in each of six independent experiments. Paired Student's *t*-tests were performed.

H Images of Bem1-GFP (cyan) and Cdc24-mCherry (red) signals in *cho1*Δ *9xMyc-AID-stt4* cells with or without auxin. Images display maximum intensity projections of *z*-stacks.

I Maximum intensity projections of *z*-stacks displaying Bem1-GFP in the mutants indicated. Bem1-GFP was imaged in *mss4-102 cho1*Δ cells after shifting to the restrictive temperature for 30 min.

J Frequency of cells with polarized Bem1-GFP signal after incubation at the time and temperature shown. Values are means ± SD, $n > 200$ cells in each of three independent experiments. Paired Student's *t*-tests were performed.

Data information: $^{**}P < 0.01$, $^{***}P < 0.001$, $^{****}P < 0.0001$. Scale bars = 2 μm.

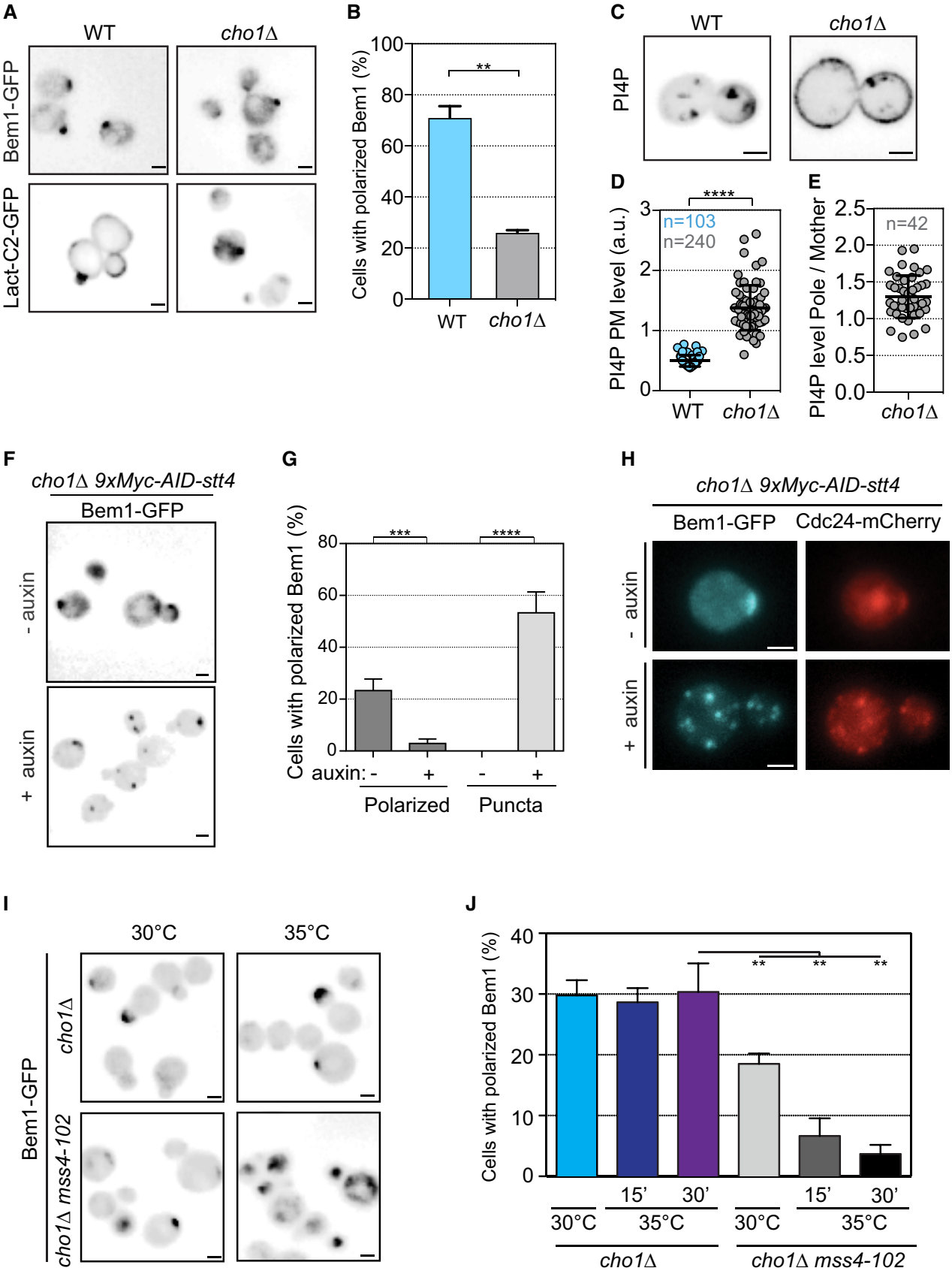
A
WT
cho1Δ
Bem1-GFP
Lact-C2-GFP
B
Cells with polarized Bem1 (%)
**
WT
cho1Δ
C
WT
cho1Δ
PI4P
D
PI4P PM level (a.u.)
****
n=103
n=240
WT
cho1Δ
E
PI4P level Pole / Mother
n=42
cho1Δ
F
cho1Δ 9xMyc-AID-stt4
Bem1-GFP
- auxin
+ auxin
G
Cells with polarized Bem1 (%)
***
****
auxin: - + - +
Polarized
Puncta
H
cho1Δ 9xMyc-AID-stt4
Bem1-GFP
Cdc24-mCherry
- auxin
+ auxin
I
30°C
35°C
Bem1-GFP
cho1Δ
cho1Δ mss4-102
J
Cells with polarized Bem1 (%)
**
**
**
15'
30'
15'
30'
30°C
35°C
30°C
35°C
cho1Δ
cho1Δ mss4-102

Figure 1.

auxin treatment, consistent with its degradation (Fig EV1I). The percentage of cells displaying polarized Bem1-GFP when PI4P and PS were ablated dropped from 25 to 3%. Upon PS and PI4P attenuation, Bem1-GFP accumulated in puncta in 55% of cells (Fig 1F and G). Simultaneous imaging of the GEF Cdc24-mCherry and Bem1-GFP indicated that the Bem1-GFP puncta also contained the GEF, reflecting association of the two proteins in a protein complex (Fig 1H).

Since PI4P is a precursor of PI(4,5)P2, the ablation of plasma membrane PI4P also reduces PI(4,5)P2 levels. We therefore tested whether direct reduction of PI(4,5)P2 using the temperature sensitive *mss4-102* allele affected Bem1 localization (Stefan *et al*, 2002). We observed that the percentage of cells displaying polarized Bem1-GFP was reduced from around 80% to around 50% when *mss4-102* cells were switched to the restrictive temperature (Fig EV1J). This is consistent with a previous report that Cdc42 is also mislocalized upon *MSS4* inactivation (Yakir-Tamang & Gerst, 2009). As was the case for PI4P, the simultaneous ablation of PS and PI(4,5)P2 resulted in the severe mislocalization of Bem1-GFP; only 7% of cells displayed polarized Bem1-GFP after 15 min at the restrictive temperature (Fig 1I and J). The inactivation of PI4P production at the Golgi using the *pik1-139* allele did not result in Bem1-GFP mislocalization (Fig EV1J; Sciorra *et al*, 2005). As additional controls for these experiments, we observed a reduction in the plasma membrane levels of PI(4,5)P2 and PI4P probes in the *mss4-102 cho1*Δ mutant at the restrictive temperature (Fig EV1K and L). We also observed a reduction in the plasma membrane levels of a PI(4,5)P2 probe in the AID-*stt4 cho1*Δ mutant treated with auxin (Fig EV1M). These results underscore the key role of PS and plasma membrane phosphoinositides in the localization of Bem1 and Cdc24 *in vivo*, and the importance of these anionic lipids in the spatial control of Cdc42 activation.

Identification of a robust anionic lipid targeting sequence in Bem1

Previously, the PX domain of Bem1 was shown to interact directly with anionic lipids; however, it is unknown whether the interaction is sufficiently robust to target the full-length protein to these lipids (Yu & Lemmon, 2001; Stahelin *et al*, 2007). We established liposome floatation assays to address this question. In the assay, liposomes were mixed with Bem1 purified from bacteria and floated through dense sucrose. In the event of a sufficiently strong interaction, the protein is found in the supernatant, associated with the liposomes (Fig 2A). A panel of neutral to anionic lipids was tested. While BSA did not interact appreciably with any of the lipids (Fig EV2A), Bem1 displayed a robust interaction with anionic liposomes. Strikingly, liposomes containing 20% PS, 5% PI4P, and 75% PC or 20% PS, 5% PI(4,5)P2, and 75% PC, resembling the composition of the plasma membrane (PM lipids), recruited more than 90% of the Bem1 in the assay, indicating that the full-length protein binds strongly to these lipids in the absence of additional proteins (Fig 2B). Bem1 interacted equally robustly with anionic liposomes containing ergosterol, the major plasma membrane sterol in yeast (Fig 2C).

The region of Bem1 responsible for the PS-PI4P lipid interaction was next mapped (Fig 2D). While the PX domain interacted weakly with PM lipids in the assay (16% floatation), an N-terminal 72 amino acid sequence interacted more strongly with this lipid mix (41% floatation; Fig 2E, mauve bar). The sequence was enriched in clusters of basic residues that we refer to as basic cluster (BC) motifs (Fig EV2B).

We next tested the effects of the BC motifs on lipid organization by mixing liposomes with the BCs and analyzing the interaction using ^{2}H solid-state NMR spectroscopy. The Bem1 BC motifs had little impact on lipid acyl chains in liposomes containing PC alone using 28 carbon acyl chains (DMPC). However, in the presence of anionic liposomes composed of PC/PS/PI4P containing DMPC and DMPS, Bem1 BCs increased ordering of the labeled acyl chains, reflected by the higher order parameters (Fig EV2C). We next increased the acyl chain length to 34 carbons using POPC and POPS, which more closely resembles the bulk acyl chain lengths of the yeast plasma membrane. Here, the BC motifs had little effect on PC/PS alone, as reflected in the overlapping signals (Fig 2F). However, in the presence of PC/PI4P and PC/PS/PI4P we observed a subtle, though significant trend toward acyl chain ordering from carbons 2-11 that was absent with PC/PS/PI(4,5)P2 liposomes (Figs 2G and H, and EV2D). Interestingly, the Bem1 BC motifs had the opposite

Figure 2. Identification of basic cluster motifs in Bem1 and their effect on the ordering of lipid acyl chains.

A Schematic of the liposome floatation assay. In the assay, liposomes of defined lipid composition were floated through a dense sucrose gradient by ultracentrifugation. Protein that associates with the liposomes is enriched in the supernatant.

B Upper panel: SDS–PAGE stained with Coomassie blue in which Bem1 is indicated. Lower panel: The liposomes were composed of 100% phosphatidylcholine (PC), 80% PC and 20% phosphatidylethanolamine (PE), 95% PC and 5% phosphatidic acid (PA), 95% PC and 5% phosphatidylinositol (PI), 95% PC and 5% PI(4,5)P2 (PI(4,5)P2), 95% PC and 5% PI4P (PI4P), 80% PC and 20% phosphatidylserine (PS), or 75% PC 20% PS 5% PI4P (PS+PI4P). (S) supernatant, (P) pellet.

C Liposomes composed of either 100% PC ± 40% ergosterol or 75% PC, 20% PS, 5% PI4P ± 40% ergosterol replacing PC were incubated with Bem1 and treated as in panel (B).

D Scheme of full-length Bem1 with its domains and the Bem1 deletion constructs used to identify the anionic lipid interacting sequences.

E Percentage of the indicated bem1 constructs associated with liposomes containing 75% PC, 20% PS, and 5% PI4P.

F Lipid ordering determined by ^{2}H solid-state NMR analysis of liposomes containing POPC-d31/POPS (4:1 molar ratio) in the presence or absence of Bem1 BC motifs. Calculation of oriented-like spectra from Pake patterns (de-Pake-ing) and simulation of ^{2}H solid-state NMR spectra were applied to measure individual quadrupolar splittings for POPC-d31 and determine order parameter accurately.

G As in panel (F), containing POPC-d31/PI4P (19:1 molar ratio).

H As in panel (F), containing POPC-d31/POPS/PI4P (15:4:1 molar ratio).

I As in panel (F), containing POPC-d31/POPS/Yeast lipid extract/ergosterol (1:1:1:2 molar ratio).

Data information: Values are means ± SD, floatation assays were performed in triplicate in at least three independent experiments. Paired Student's *t*-tests were performed. $^{**}P < 0.01$, $^{***}P < 0.001$, $^{****}P < 0.0001$.
Source data are available online for this figure.

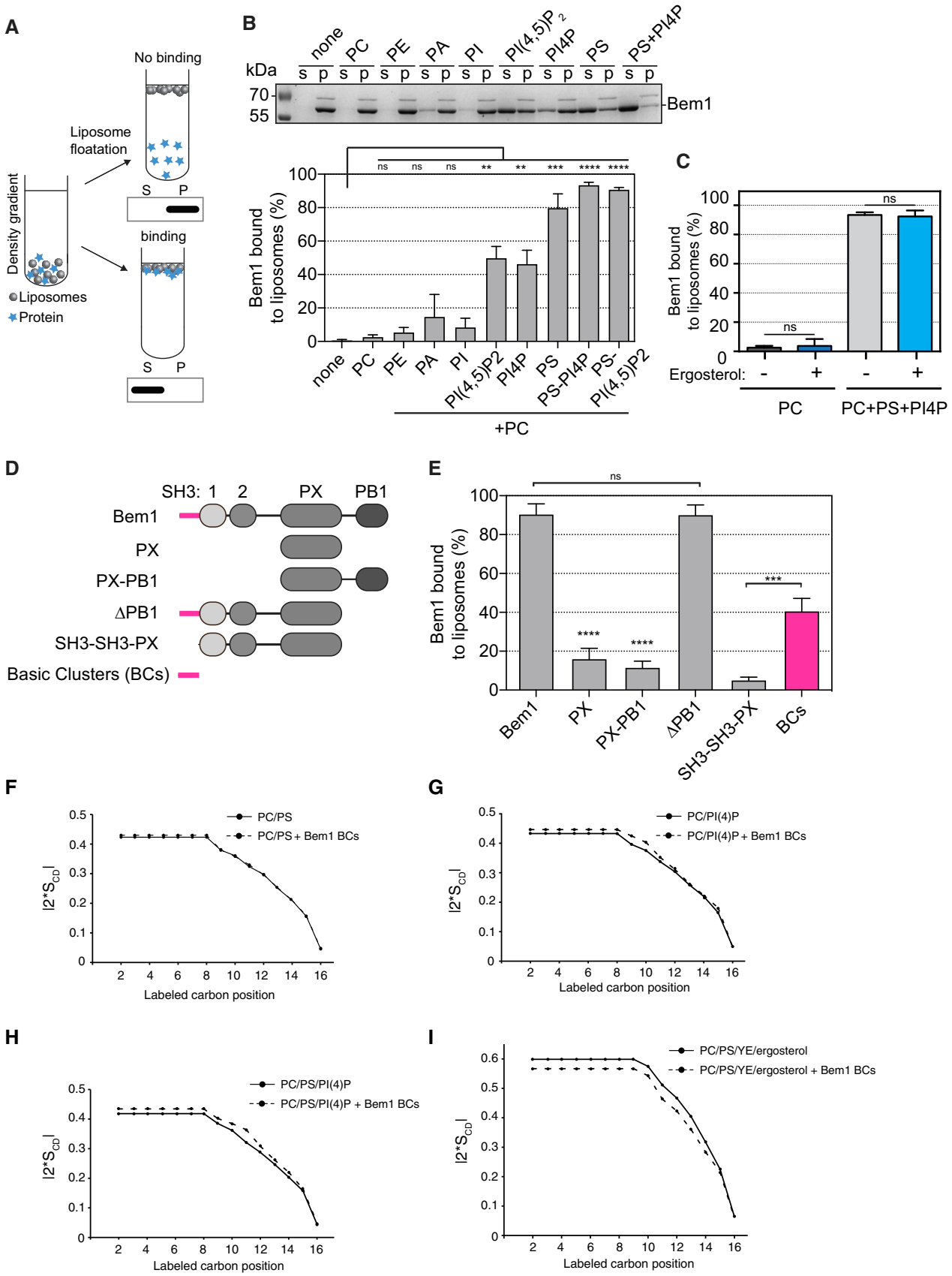
A
No binding
Liposome floatation
Density gradient
binding
Liposomes
Protein
S P
B
kDa
70
55
Bem1
none PC PE PA PI PI(4,5)P2 PI4P PS PS+PI4P
Bem1 bound to liposomes (%)
+PC
C
Ergosterol:
PC
PC+PS+PI4P
D
SH3: 1 2 PX PB1
Bem1
PX
PX-PB1
ΔPB1
SH3-SH3-PX
Basic Clusters (BCs)
E
F
PC/PS
PC/PS + Bem1 BCs
|2*SCD|
Labeled carbon position
G
PC/PI(4)P
PC/PI(4)P + Bem1 BCs
H
PC/PS/PI(4)P
PC/PS/PI(4)P + Bem1 BCs
I
PC/PS/YE/ergosterol
PC/PS/YE/ergosterol + Bem1 BCs

Figure 2.

effect on acyl chain ordering, increasing the fluidity of the acyl chains in PC/PS/PI4P liposomes in the presence of ergosterol, a major regulator of plasma membrane fluidity. This effect was observed in the presence or absence of yeast extract lipids, validating our choice of lipid system (Figs 2I and EV2E). However, ergosterol had only very minor fluidizing effects on Bem1 in the presence of PI(4,5)P2 (Fig EV2F). These results indicate that Bem1 interacts with anionic lipids via clusters of basic residues, and in doing so, Bem1 may in turn influence the ordering of the acyl chain backbone in a manner dependent upon the ergosterol content of the lipid environment. Since ergosterol organization in the yeast plasma membrane is heterogenous (Grossmann *et al*, 2007), the effects of Bem1 on acyl chain ordering may also be local, that is, in regions containing low or high ergosterol.

The Bem1 BC motifs can act as a heterologous plasma membrane targeting signal *in vivo*

The N-terminus of Bem1 contains three clusters of basic residues, or BC motifs, totaling 14 lysine and arginine residues. We mutated each cluster individually or all 14 residues simultaneously (Fig 3A). We first performed liposome floatation assays to identify the BC motif that contributed most to Bem1 anionic lipid targeting. Of the three clusters of basic residues, the most N-terminal BC-1 cluster appeared to be the most important (Fig 3B). In addition, mutation of all basic residues to alanine (*bc*-14A) or a charge swap to glutamate (*bc*-14E) strongly attenuated the interaction of these full-length Bem1 constructs with PM lipids *in vitro*. We next verified that the resulting bc-14E mutant protein retained the ability to boost Cdc24 GEF activity in a GEF assay, and had thus not been non-specifically damaged by the charge-swap mutations. This FRET-based mant-GTP loading assay serves as a sensitive readout for Bem1 function, since Bem1 boosts GEF activity via interactions with Cdc24 and Cdc42 that are distinct from the N-terminal BC motifs (Ito *et al*, 2001; Yamaguchi *et al*, 2007; Rapali *et al*, 2017). The bc-14E mutant was chosen for these experiments because it was expressed at similar levels to wild-type Bem1 *in vivo*, as demonstrated below. In these assays, the bem1 bc-14E mutant and wild-type Bem1 boosted Cdc24 GEF activity indistinguishably, consistent with the idea that mutation of the basic clusters had not resulted in non-specific Bem1 mis-folding, (Figs 3C and EV3A).

The BC motifs in Bem1 are necessary for the interaction with anionic lipids, but are they sufficient? We tested whether a single BC motif in Bem1 was sufficient for heterologous targeting of proteins to the plasma membrane *in vivo*. The viability of budding yeast requires a Cdc42 C-terminal polybasic sequence containing four lysines that interact with anionic lipids, providing an *in vivo* system in which to test the functional importance of a single BC motif (Kozminski *et al*, 2000). We generated budding yeast in which the wild-type copy of *CDC42* was expressed from the conditional *GAL1* promoter. Expression of wild-type *CDC42* was repressed by plating cells on dextrose and then we tested whether the most N-terminal Bem1 BC-1 motif could support the viability of the *cdc42* polybasic mutant when engineered onto the C-terminus of cdc42 immediately preceding the geranylgeranylation site. While the *cdc42* polybasic mutant was unable to support cellular viability when grown on dextrose, as indicated by the lack of colony growth on dextrose plates (Fig 3D, blue box), appending the Bem1 BC-1 motif to this mutant restored viability, albeit with a reduced rate of colony formation compared to wild-type control cells (Fig 3D, red box). Control experiments indicated that the loss of *CDC42* function required mutation of all four C-terminal lysines (Fig EV3B). The BC-1 motif was also sufficient to target the polybasic *cdc42* mutant to the plasma membrane in an anisotropic manner (Fig 3E, red box). In addition, the BC-1 motif interacted with PC/PS/PI4P lipids in the liposome floatation assay (Fig EV3C and D). These results indicate that the BC motifs are necessary for the strong interaction between Bem1 and anionic lipids in the reconstituted assay, and that the affinity of the single BC-1 motif for these lipids is sufficient to support viability when heterologously appended to a *cdc42* lipid-binding mutant *in vivo*.

The Bem1 BC motifs are required for Bem1 targeting to the cell pole *in vivo*

We next addressed the importance of the anionic lipid targeting BC motifs within Bem1 *in vivo*. Since previous work demonstrated that the PX domain in Bem1 was only important for the localization of the protein when additional pathways that guide polarity were also inactivated (Irazoqui *et al*, 2003), we reasoned that the PX domain may function with the BC motifs in a multivalent fashion to confer robust membrane targeting. The importance of the BC and PX membrane targeting sequences was tested *in vivo* by replacing the wild-type copy of *BEM1* with the *bem1 bc-14E* mutant, a *bem1 px* domain mutant (K338M, K348A, R349A, R369A; Stahelin *et al*, 2007), or a mutant in which both sequences were mutated. As a measure of Bem1 function, the rate of colony formation at 37°C was observed, since *bem1*Δ cells display a growth defect at this temperature that has been attributed to defective organization of the actin cytoskeleton (Bender & Pringle, 1991; Chant *et al*, 1991). While the *bem1 px* mutant displayed a rate of colony formation indistinguishable from wild-type cells, the *bem1 bc-14E* mutant displayed a reduced rate, which was exacerbated in the double *bem1 bc-14E px* mutant (Fig 4A). The mutant proteins were not non-specifically destabilized by the mutations, since 3xHA-tagged mutants were expressed comparably to wild-type Bem1-3xHA (Fig 4B).

The percentage of cells displaying polarized GFP fluorescence was reduced in the *bem1 bc-14E-GFP* mutant compared to wild type, and even more diminished in the *bem1 bc-14E px-GFP* double mutant (77% wild type, 49% *bc-14E*, and 41% *bc-14E px* double mutant; Fig 4C and D). Moreover, the intensity of GFP fluorescence at the pole in single cells indicated that all three mutants displayed significantly reduced levels of GFP signal compared to wild-type cells (Fig 4E). These results, which are consistent with our reconstitution experiments, identify the importance of the BC motifs in targeting Bem1 to the cell pole *in vivo*.

Multivalent protein–lipid interactions drive avid targeting of the GTPase module to anionic lipids *in vitro* and *in vivo*

Previous work reported that the GEF Cdc24 is targeted to, but not maintained at, the pole in *bem1Δ* mutants (Butty *et al*, 2002). Conversely, Bem1 polarization is not maintained in *cdc24* mutants (Butty *et al*, 2002), suggesting that Cdc24 may display some affinity for lipids *in vivo*, likely via its PH domain (Yu *et al*, 2004). This led us to test whether multivalent protein–lipid interactions in Bem1

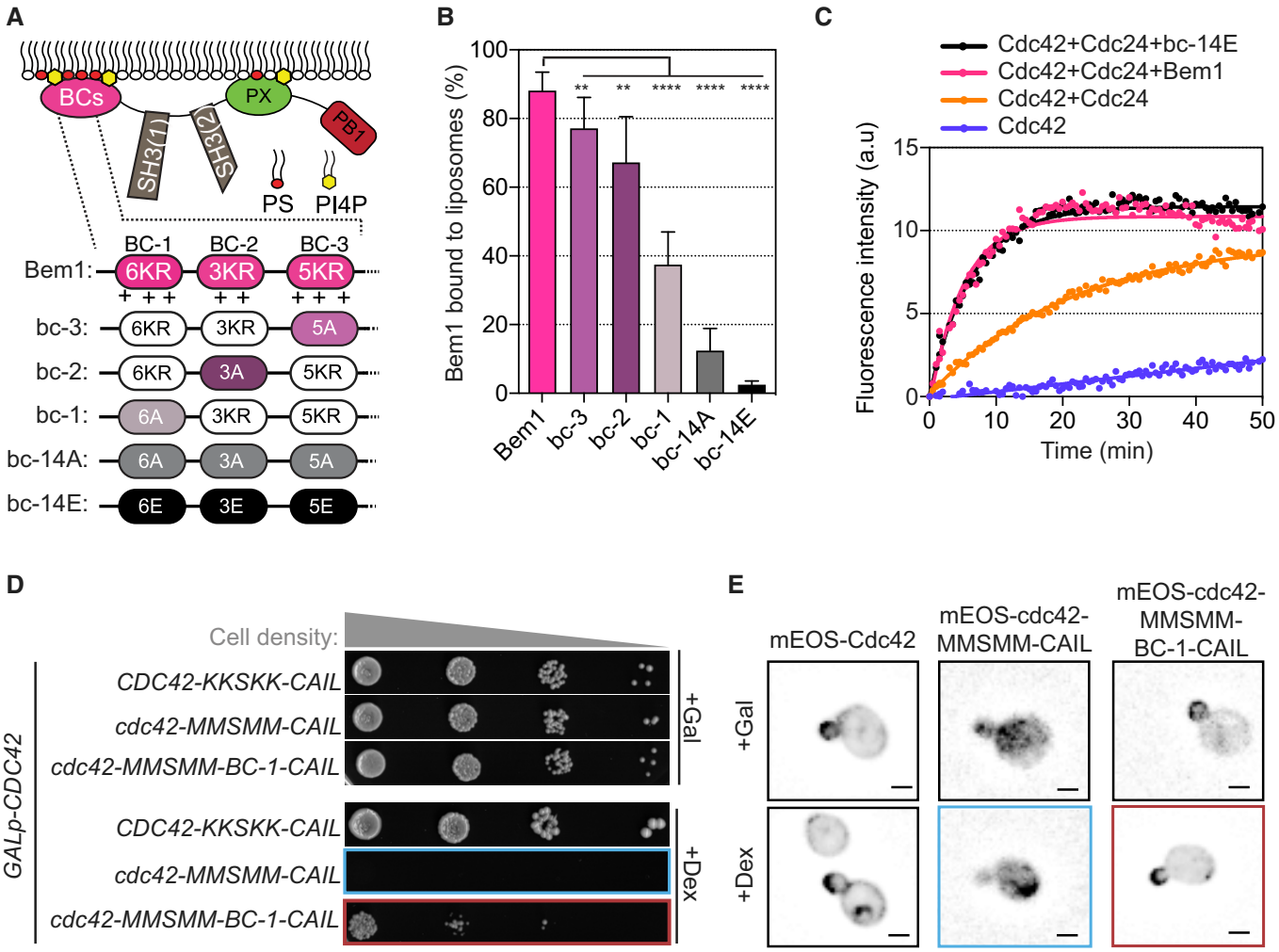

Figure 3. The Bem1 BC sequence can act as a heterologous plasma membrane targeting signal *in vivo*.

A Schematic showing Bem1 domains with the lipid interacting motifs including the BC motifs and the PX domain. The Bem1 N-terminus contains three BC motifs. The first cluster (BC-1) is composed of six K/R residues, the second cluster (BC-2) of three K/R residues, and the third cluster (BC-3) of five K/R residues. The scheme shows the full-length bem1 constructs where none, one, or all BCs were mutated.

B Percentage of the different full-length bem1 bc mutants associated with liposomes containing 75% PC, 20% PS, and 5% PI4P.

C Fluorescence intensity change associated with the nucleotide exchange of GDP-Cdc42 for mant-GTP Cdc42. Fluorescence was measured after the addition of GDP-Cdc42 to reactions containing Mant-GTP (100 nM), GMP-PNP (100 μM), and the proteins indicated.

D Tenfold serial dilutions of cells and subsequent colony formation on the indicated plates, where expression of wild-type *GALp-CDC42* is either induced in the presence of Gal or repressed in Dex. Note how mutation of the wild-type Cdc42 (KKSKK) to MMSMM is lethal (see blue box), whereas appending the Bem1 BC-1 motif to this *cdc42* mutant restores viability (red box).

E Representative images of the mEOS-cdc42 mutants signal (blue) after inducing the expression of *GAL1p-CDC42* in the presence of Gal or repressing it in the presence of Dex. The cells in the blue and red boxes correspond to the cells in the blue and red boxes in panel (D). Images are average fluorescence intensity projections in which black and white pixels have been inverted.

Data information: Values are means ± SD, floatation assays were performed in triplicate in at least three independent experiments. Paired Student's *t*-tests were performed. $^{**}P < 0.01$, $^{****}P < 0.0001$. Scale bars = 2 μm.

and Cdc24 may drive recruitment of the GEF–scaffold complex to the pole (Fig 5A). First, we tested whether Cdc24 has appreciable affinity for anionic lipids in the liposome floatation assay. Approximately 33% of Cdc24 interacted with PM lipids in the assay, and the association was reduced to around 15% when a mutation was introduced into a conserved cationic residue in the beta-2 sheet of the PH domain (cdc24 K513A, which we refer to as cdc24 ph; Figs 5B and EV4A; Hokanson *et al*, 2006). The addition of Bem1 dramatically increased the amount of Cdc24 associated with PM lipids from 33% to more than 88% (Fig 5C). While mutation of the BC motifs in Bem1 had the strongest impact on Cdc24 association with PM lipids, successive neutralization of the BC and PX motifs in Bem1, combined with mutation of the PH domain in Cdc24, resulted in a progressive reduction in the interaction of Cdc24 with PM lipids (Fig 5C). We directly tested whether avidity is generated via multivalent interactions by varying the concentration of Bem1 and plotting the amount of Cdc24 associated with PM lipids (Fig 5D). Fitting the curves with an equilibrium-binding model revealed that the K_d

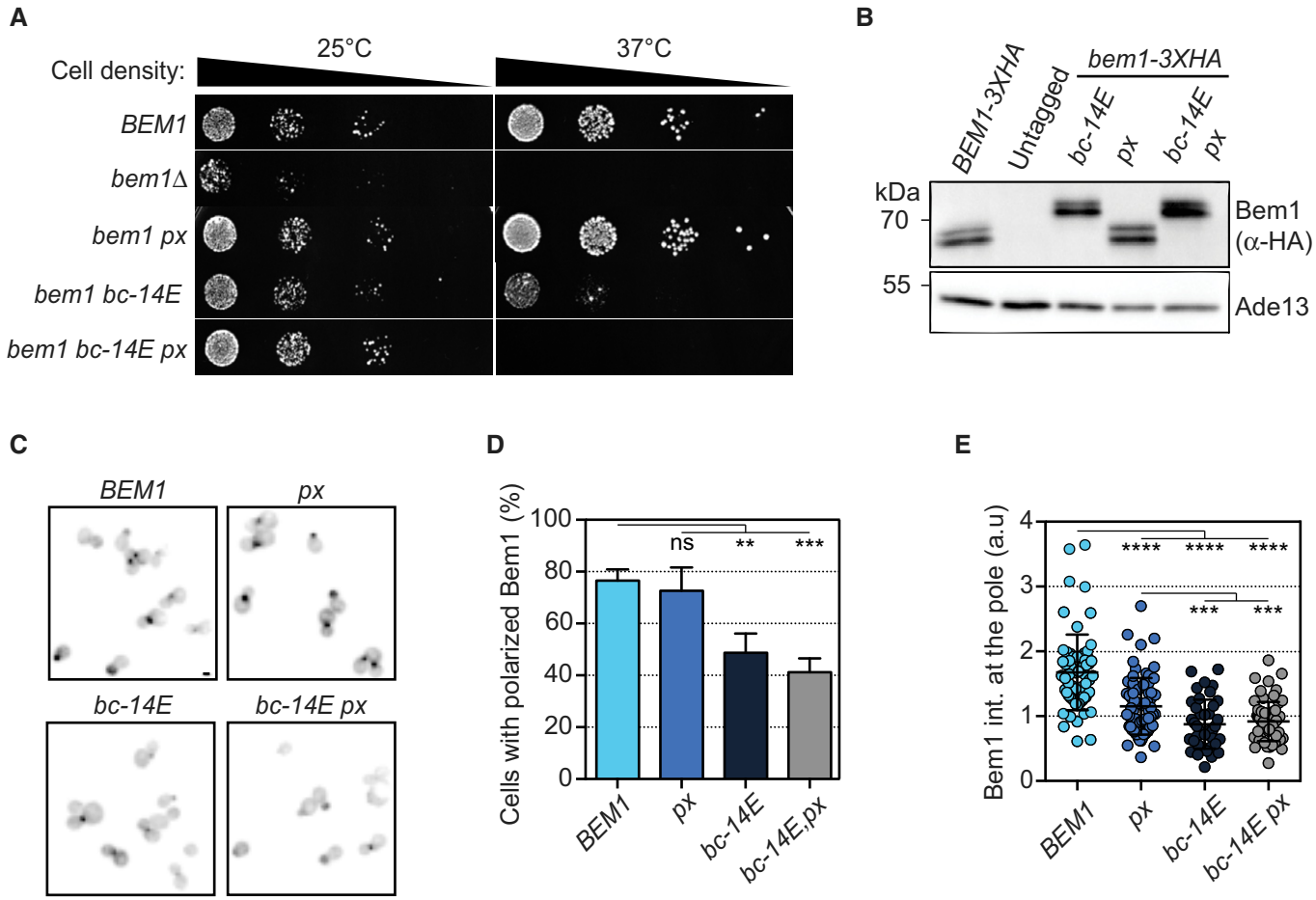

Figure 4. The Bem1 BC sequence is required for Bem1 targeting to the cell pole *in vivo*.

A Tenfold serial dilutions of the indicated mutant cells and subsequent colony formation at the temperatures indicated. Note how mutations on both the BC motifs and PX in bem1 compromise growth at the restrictive temperature.

B Western blots probed with anti-HA antibody to detect the indicated bem1 constructs tagged with 3XHA (top panel). Detection of Ade13 was used as loading control (bottom panel).

C Representative images of the indicated bem1 mutants tagged with GFP at the *BEM1* locus. The inverted fluorescence images are average intensity projections.

D Frequency of cells with polarized Bem1-GFP.

E Scatter dot plot showing the fluorescence levels of the indicated *bem1* strains at the cell pole. The measurements were made on average intensity projections.

Data information: Values are means ± SD. In panel (D), $n > 100$ cells counted in each of three independent experiments. Comparisons were made using paired Student's *t*-tests. In panel (E), $n > 100$ cells, counted in each of three independent experiments and the data were compared using a Mann–Whitney test. In panels (D and E): $^{**}P < 0.01$, $^{***}P < 0.001$, $^{****}P < 0.0001$. Scale bar = 2 μm.

Source data are available online for this figure.

of Cdc24 for anionic lipids was acutely sensitive to Bem1 lipid binding. The apparent K_d of Cdc24 for PM lipids in the presence of wild-type Bem1 was 6 nM, 117 nM in the bem1 bc-14A mutant, and 180 nM in the bem1 bc-14A px mutant. These results indicate that multivalent lipid-binding motifs in Bem1, conferred by the BC motifs and PX domain, contribute to the avid targeting of Cdc24 GEF activity to anionic lipids in the reconstituted system. Of these interactions, the BC motifs that we identify in Bem1 provide the strongest anionic lipid targeting to the GEF–scaffold complex. These results are consistent with a model of GEF–scaffold targeting via multivalent anionic lipid avidity.

The multivalent avidity model was next tested *in vivo*. Mutation of the Bem1 BC motifs, PX domain, and the Cdc24 PH domain resulted in a progressively more pronounced temperature sensitive phenotype (Fig 5E). Importantly, by appending a geranylgeranylation sequence to these mutants, it was possible to restore growth at 37°C, indicating that temperature sensitivity was a result of reduced membrane targeting and not non-specific protein mis-folding due to mutation (Fig EV4B). Morphological defects consistent with a loss of cell polarity in the mutants also became more severe as additional mutations in the identified lipid tethering motifs were combined, even at 25°C (Fig 5F). We addressed whether the loss of cellular polarity observed *in vivo* was associated with specific Cdc42 signaling pathway defects. Cdc24 multisite phosphorylation by the p21 activated kinase (PAK) Cla4 occurs optimally in the presence of Bem1 when Cdc24 is localized on the plasma membrane (Gulli *et al*, 2000; Butty *et al*, 2002; McCusker *et al*, 2007; Rapali *et al*, 2017). We therefore predicted that Cdc24 might display aberrant

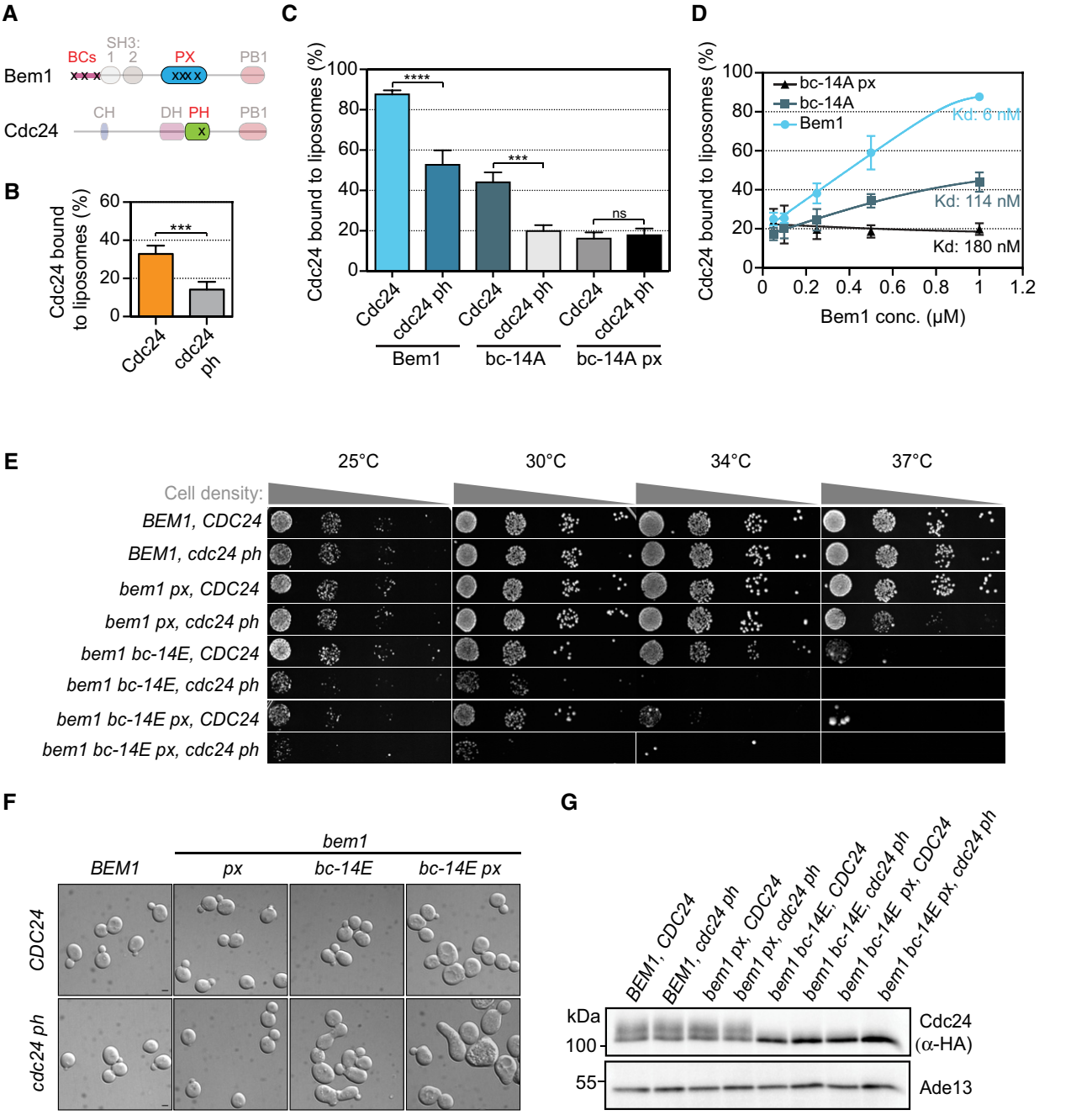

Figure 5. Multivalent protein–lipid interactions drive avid targeting of the Bem1-Cdc24 complex to anionic lipids.

A Scheme of Bem1 and Cdc24 proteins indicating the relative position of the mutations in the lipid tethering motifs (black x).

B Percentage of full-length Cdc24 and cdc24 ph domain mutant (cdc24 ph) associated with liposomes containing 75% PC, 20% PS, and 5% PI4P.

C Percentage of Cdc24 and cdc24 ph mutant associated with liposomes of the composition shown in (B) in the presence of the indicated bem1 protein. Note how additive mutations in the Bem1 lipid-binding sequences reduce the percentage of Cdc24 associated with the liposomes.

D Percentage of Cdc24 and cdc24 ph associated with liposomes of the composition shown in (B) as a function of the indicated bem1 protein concentration. The curves denote the regression fit of the data to equation 2 in the Materials and Methods.

E Tenfold serial dilutions and subsequent colony formation of the indicated mutant cells at the indicated temperatures.

F DIC images of the indicated bem1 and cdc24 mutants showing the increased morphological defects ensuing from loss of lipid tethering in the *bem1* and *cdc24* mutants.

G Western blots probed with anti-HA antibody to detect Cdc24 or cdc24 ph tagged with 3XHA in the indicated mutant strains (top panel). Detection of Ade13 was used as a loading control (bottom panel).

Data information: Values are means ± SD, floatation assays were performed in triplicate in at least three independent experiments. Paired Student's *t*-tests were performed. ***$P < 0.001$, ****$P < 0.0001$. Scale bars = 2 μm.
Source data are available online for this figure.

phosphorylation in the GEF–scaffold lipid-binding mutants. Consistently, Cdc24 phosphorylation was observed to be dramatically reduced in the *bem1 bc-14E* mutant, and all combinations thereof, as indicated by the increased hypophosphorylated form of Cdc24 in electrophoretic mobility shifts during SDS–PAGE (Fig 5G). These results indicate that the BC motifs identified in Bem1 and the multivalent anionic lipid interactions displayed by the GEF–scaffold complex are required for the spatial control of Cdc42 activation, signaling via PAK, and the ensuing control of cellular polarity.

Scaffold tethering to anionic lipids affects Cdc42 dynamics and activation *in vivo*

The loss of cell polarity ensuing from reduced Bem1 tethering to the plasma membrane suggested that Cdc42 dynamics would be altered in the *bem1 bc-14E* mutant. At the cell pole in wild-type cells, Cdc42 displays reduced diffusion compared with elsewhere on the plasma membrane, reflecting activation of Cdc42 at the cell pole (Slaughter *et al*, 2013; Sartorel *et al*, 2018). Previous work from our laboratory demonstrated that Bem1, which boosts Cdc42 activation (Rapali *et al*, 2017), and PS, which recruits Cdc42 activators, contribute to the reduced diffusion and nanoclustering of Cdc42 at the pole (Sartorel *et al*, 2018). We therefore reasoned that the reduced rate of Cdc42 diffusion and its nanoclustering at the pole may be linked to the lipid interactions exhibited by the Bem1 BC motifs. To test this hypothesis, we monitored mEOS-Cdc42 dynamics in live wild-type, *bem1 bc-14E,* and *bem1 bc-14E px* mutant cells by single-particle tracking photoactivation localization microscopy (sptPALM; Fig 6A). From high-frequency sptPALM acquisitions (50 Hz), trajectories were obtained from mEOS-Cdc42 at the pole and non-pole regions of cells. The mean square displacement of the protein, which is a measure of Cdc42 mobility, was extracted from the assembled single-molecule tracks. In wild-type cells, mEOS-Cdc42 displayed more confinement at the pole than at the non-pole, as expected. However, reduced mobility of mEOS-Cdc42 was not observed at the pole of *bem1 bc-14E* and *bem1 bc-14E px* mutants (Fig 6B). This was also borne out quantitatively by calculating the diffusion coefficient, *D*, from the slope of the MSD curves (Fig 6C). We next fixed cells and looked at the organization of mEOS-Cdc42 by PALM. Whereas mEOS-Cdc42 nanoclusters were larger at the pole of wild-type cells, we observed no difference in the size of mEOS-Cdc42 nanoclusters between the pole and non-pole of *bem1 bc-14E px* mutant cells (Fig 6D and E). These results indicate that the interaction between the BC motifs in Bem1 and anionic lipids is required for the reduced diffusion of Cdc42 and its organization in large nanoclusters at the pole. In order to directly link the alteration in Cdc42 nanoclustering with Bem1 lipid tethering and Cdc42 activation, we monitored Cdc42-GTP levels by quantitative imaging using a $gic2_{(1–208)}$-yeGFP probe, which contains a CRIB motif that interacts with the active GTPase. The levels of the probe were reduced in the *bem1 bc-14E* and *bc-14E px* mutant compared to a wild-type control (Fig 6F). Collectively, these results indicate that Bem1 lipid tethering via the BC motifs is required for three key properties of Cdc42 at the cell pole: its reduced diffusion, its organization in large nanoclusters, and its optimal activation.

Discussion

The mechanisms underlying the targeting of the Cdc42 regulators Bem1 and Cdc24 to the plasma membrane represent a longstanding enigma, despite the budding yeast polarity system being one of the most intensively studied among eukaryotes. Previous studies in diverse experimental models have highlighted a crucial role for positive feedback in amplifying the levels of active polarity factors at the cell pole during polarity axis establishment (Weiner *et al*, 2002; Snaith & Sawin, 2003; Srinivasan *et al*, 2003; Wedlich-Soldner *et al*, 2004; Fletcher *et al*, 2012). In budding yeast, Bem1 is proposed to play a role in this feedback (Bose *et al*, 2001; Goryachev & Pokhilko, 2008; Witte *et al*, 2017); however, the mechanisms that localize Bem1 to the plasma membrane to trigger the positive feedback have been enigmatic. Combining the rapid ablation of plasma membrane lipids *in vivo* with a sensitive reconstituted system, we identify a mechanism underlying the spatial tethering of Bem1 and the GEF Cdc24 to anionic lipids enriched at the cell pole via multivalent interactions (Fig 7). Moreover, our solid-state NMR spectroscopy experiments suggest that the interaction between Bem1 and anionic lipids is reciprocal in the sense that Bem1 influences the ordering of lipid acyl chains, rigidifying the local membrane environment where ergosterol levels are low, while fluidizing it where ergosterol levels are high. Interestingly, ergosterol levels have been reported to be non-homogeneous in the yeast plasma membrane, where it was observed to cluster, although another study reported a more homogeneous distribution (Grossmann *et al*, 2007; Solanko *et al*, 2018).

Previous studies identified an important role for the anionic lipid PS in the anisotropic plasma membrane recruitment of Cdc42 and its regulator Bem1, although the underlying mechanism was unknown (Fairn *et al*, 2011). While the PX domain of Bem1 interacts with PS *in vitro*, mutation of the relevant cationic residues in the Bem1 PX domain did not result in a phenotype unless additional pathways that guide polarity were also inactivated *in vivo* (Irazoqui *et al*, 2003; Stahelin *et al*, 2007). It was therefore unknown if additional lipid-binding sites existed in Bem1. We demonstrate that Bem1 does indeed employ a second anionic lipid region composed of BC motifs, which together with the PX domain, mediates the robust interaction of Bem1 with negatively charged lipids.

Five lines of evidence support the involvement of the BC motifs in the anionic lipid targeting of Bem1. First, mutation of the cationic residues that constitute the motifs dramatically reduced the affinity of Bem1 for these lipid species in a reconstituted system. Second, a BC motif construct was sufficient to interact with liposomes mimicking plasma membrane lipid composition. Third, appending a single *BC* motif to a *cdc42* mutant that is defective in anionic lipid recruitment is sufficient to restore viability to this otherwise lethal mutant *in vivo*. While the addition of exogenous Lyso-PS to this mutant did not restore the rate of colony formation to wild-type levels in our experiments, this may reflect the difference in acyl chain composition between PS and Lyso-PS. Fourth, mutation of the *BC* motifs reduces the localization of Bem1 to the cell pole at a population and at a single cell level *in vivo*. Finally, as discussed below, solid-state NMR data indicate a specific interaction between Bem1 and anionic lipids.

Anionic lipids recruit Bem1 and this interaction may influence the ordering of the lipid acyl chain backbone in a PS-PI4P-dependent

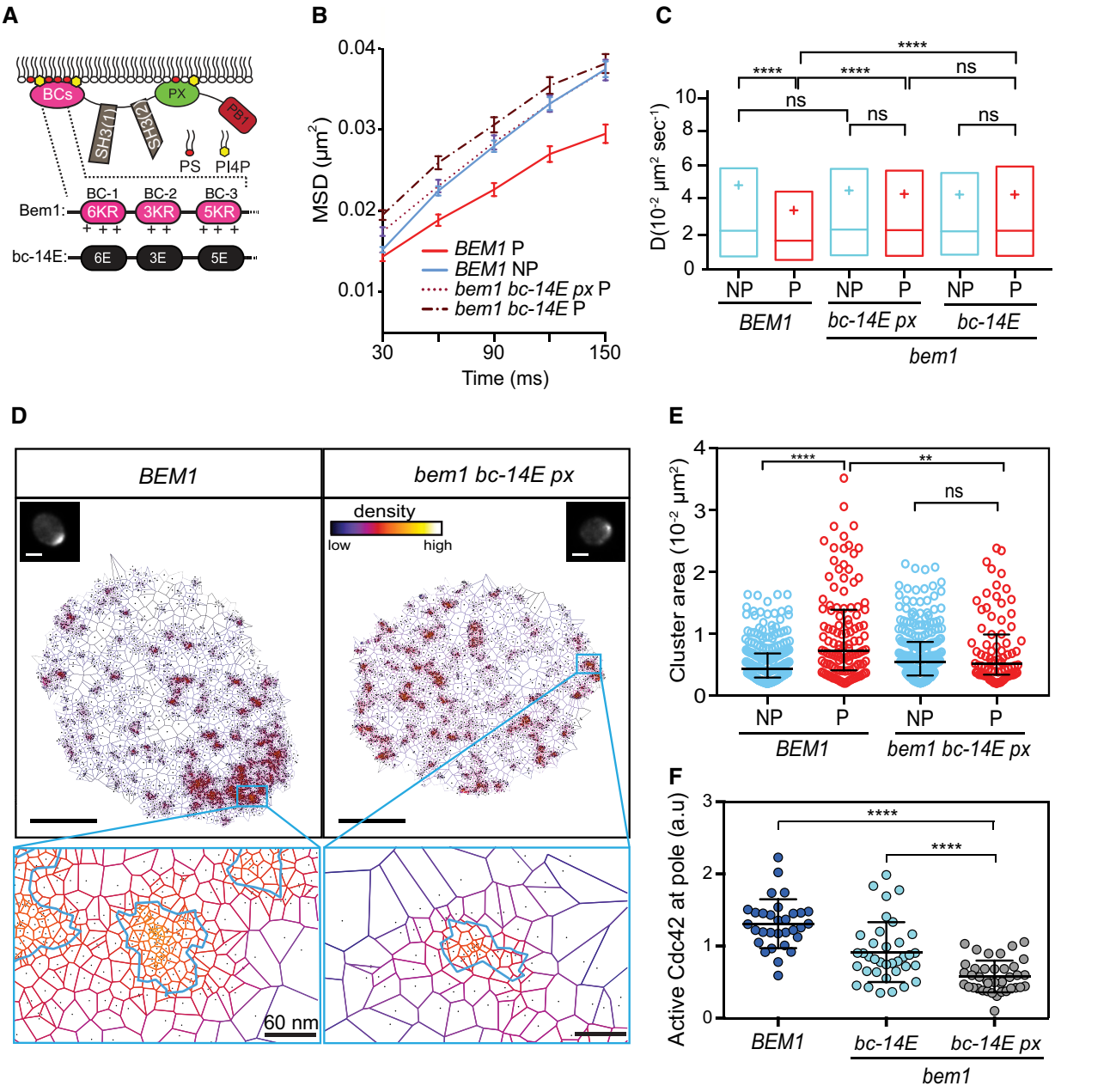

Figure 6. The Bem1 BC motifs are required for reduced Cdc42 diffusion, large nanoclusters, and optimal Cdc42 activation at the cell pole.

A Scheme of the *bem1* mutants used for imaging.

B Global average MSD curves of mEOS-Cdc42 in the strains indicated at the pole (P) and non-pole (NP) of cells. Trajectories longer than six frames were analyzed. Number of trajectories analyzed: *BEM1* (n = 11 cells: non-pole: 1,814 tracks; pole: 706); *bem1 bc-14E px* (n = 10 cells: non-pole: 1,793 tracks; pole: 908); *bem1 bc-14E* (n = 13 cells: non-pole: 1714 tracks; pole: 975). Error bars display SEM.

C *D* coefficients of mEOS-Cdc42 in the strains indicated (in box plots displaying the median (line), the 25–75 percentiles (box), and the mean (cross)), which were compared using a non-parametric, two-tailed Mann–Whitney rank sum test.

D SR-Tesseler images of mEOS-Cdc42 nanocluster organization in *BEM1* (5,312 localizations shown in image) and *bem1 bc-14E px* cells (3,739 localizations shown). Insets show mEOS-Cdc42 after 491-nm widefield laser excitation to identify the cell pole. Scale bars: 2 μm. A zoom of the pole region shows the organization of the detected nanoclusters, circled in light blue, in the strains indicated. Scale bar in the zoom: 60 nm.

E Distribution of nanocluster area at the pole (P) and non-pole (NP) regions of *BEM1* (diameter NP: 59 nm ± 1 nm (SEM); P: 74 nm ± 3.2 nm; n = 16 cells. NP: 570 clusters; P: 162 clusters) and *bem1 bc-14E px* cells (diameter NP: 59 nm ± 1.5 nm (SEM); P: 57 nm ± 2.4 nm; n = 15 cells. NP: 421 clusters; P: 141 clusters). Data are presented as scatter dot plots displaying the median as a line and the 25–75 percentiles. Data were compared using non-parametric, two-tailed Mann–Whitney rank sum test.

F Active Cdc42-GTP levels were quantified in the strains indicated using a $gic2_{(1–208)}$-yeGFP probe. Values are mean ± SD for n = 30 cells observed over two experiments. Data were compared using a Mann–Whitney test.

Data information: ns, $P > 0.05$, *$P < 0.05$, **$P < 0.01$, ***$P < 0.001$, ****$P < 0.0001$.

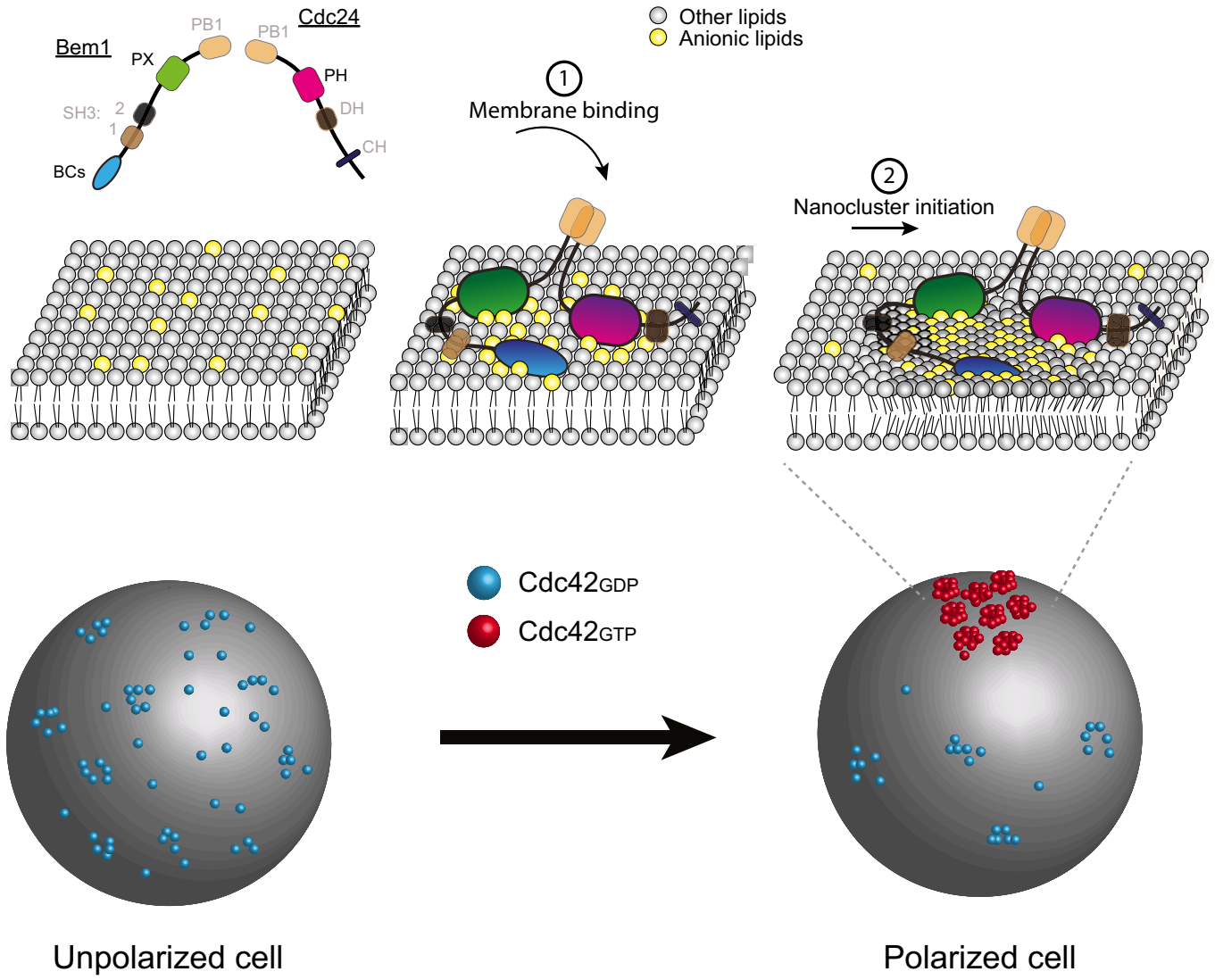

Figure 7. Schematic illustrating the relationship between Cdc42 regulators and the membrane environment during polarity establishment.

1 The Bem1-Cdc24 complex is recruited to the plasma membrane via multivalent interactions with anionic lipids. The BC motifs in Bem1 provide the strongest affinity for anionic lipids at this step.

2 Upon their recruitment to anionic lipids, the Bem1 BC motifs may influence the local membrane environment, contributing to local Cdc42 activation by Cdc24 and Cdc42 nanoclustering.

manner, increasing membrane rigidity in regions of low ergosterol. This is likely to reduce the diffusion of Cdc42 GTPase components locally. In eukaryotes, diverse Ras-family GTPases display heterogeneous diffusion on the plasma membrane, where active GTPases and other signaling proteins have been imaged in discrete sub-diffraction limited ensembles, also referred to as nanoclusters (Murakoshi *et al*, 2004; Tian *et al*, 2007; Das *et al*, 2015; Nan *et al*, 2015; Zhou *et al*, 2015, 2017; Gronnier *et al*, 2017; Remorino *et al*, 2017). Cdc42 is organized in nanoclusters that are larger at the cell pole (Sartorel *et al*, 2018), where Bem1 contributes to GTPase activation (Rapali *et al*, 2017). These larger nanoclusters at the pole require Bem1 and phosphatidylserine. Indeed, exogenous addition of PS is sufficient to induce the organization of Cdc42 into large nanoclusters, but only if Bem1 is present (Sartorel *et al*, 2018). We therefore propose that Bem1-dependent Cdc42 nanoclustering via PS is likely to be mediated by the BC motifs in Bem1. The increased membrane rigidity generated by basic cluster motifs in other proteins, combined with the potential of PS to span the two leaflets of the lipid bilayer (Raghupathy *et al*, 2015), may constitute critical ingredients for nanocluster-mediated signaling on the plasma membrane.

Taking advantage of the newly identified BC motifs in Bem1 as a starting point, we addressed more generally the mechanistic basis of GEF–scaffold anionic lipid targeting. We identified multivalency in the protein–lipid interactions as a critical constituent of avid GTPase module targeting to the plasma membrane.

Intuitively, multivalency as a means of avid protein targeting is appealing, since multiple juxtaposed ligand binding sites in a target have the potential to confer multiplicative rather than additive affinity (Kelly *et al*, 1976). Consistently, a previous study demonstrated that the electrostatic-based interaction of N-WASP with PI(4,5)P2 is multivalent, and that this contributes both to the cooperativity of this protein–lipid interaction and to the ultrasensitive, switch-like kinetics of actin polymerization (Papayannopoulos *et al*, 2005). Since polarity establishment is also a switch-like process, it is conceivable that cooperativity in the Bem1–lipid interaction may contribute to these properties. Multivalent protein–lipid interactions also underlie Par polarity complex localization to anionic lipids at the cortex, where basic-hydrophobic domains resemble the BC motifs that we identify in Bem1 (Bailey & Prehoda, 2015). Similarly, multivalent protein–lipid interactions play a role in the recruitment of dynamin, EEA1, retromer, and ESCRT-III complexes to membranes (Lemmon & Ferguson, 2000; Seaman & Williams, 2002; Hayakawa *et al*, 2004; Buchkovich *et al*, 2013). Future experiments examining the degree of lipid penetration by the membrane targeting signals in these proteins are warranted to understand whether they influence the local membrane environment.

In the case of the Cdc42 module in budding yeast, additional peripheral membrane proteins associated with Cdc24 and Bem1 are likely to contribute additional multivalent effects. For example, both Boi1 and Boi2, which interact with Bem1 and Cdc24, each contain a PH domain, as do Cdc42 GAPs (Peterson *et al*, 1994; Bender *et al*, 1996; McCusker *et al*, 2007). These proteins may increase the avidity of the Cdc42 GTPase module for anionic lipids further, or, if their affinity for other lipid species is sufficient, they may contribute additional lipid-specific targeting functions to the GTPase module.

Materials and Methods

Plasmid construction

Bem1 expression plasmids were generated using a modified pGEX6P-2 backbone in which the BamHI site in the multiple cloning site was changed to NdeI. Full-length Bem1 and the truncated proteins were amplified by PCR, introducing NdeI and XhoI restriction sites and cloned into the modified pGEX6P-2 vector to generate pDM256, pDM548, pDM514, pDM516, and pDM577, respectively. The *bem1 bc* mutants (*bc-1*, *bc-2*, *bc-3*, *bc-14A,* and *bc-14E*) were synthesized with NdeI and BamHI restriction sites (Bio-Basic, Markham, Canada). The NdeI/BamHI fragments were cloned into the modified pGEX6P-2 vector to generate pDM602 (*bc-1*), pDM604 (*bc-2*), pDM599 (*bc-3*), pDM600 (*bc-14A*), and pDM890 (*bc-14E*).

BEM1, *bem1 bc-14E,* and *bem1 bc-14E px* constructs were cloned into a yeast integrating plasmid (pRS306) containing 0.4 Kb upstream of the *BEM1* start codon and 0.143 Kb downstream of the stop codon. The *BEM1* coding sequence and mutants were ligated as XhoI–EagI fragments, generating pDM865, pDM906, and pDM947, respectively.

Table EV1 contains a list of the plasmids used in this study.

Yeast strains and growth conditions

The *cho1*Δ strains were generated by replacing the *CHO1* gene with kanMX6- or hphNT1-selectable markers (Longtine *et al*, 1998; Janke *et al*, 2004). For experiments employing the *cho1*Δ mutant, minimal medium supplement with 1 μM choline was used, except where noted. *cho1*Δ strains were routinely tested to ensure choline auxotrophy (Atkinson *et al*, 1980).

The AID-stt4 strains were generated as follows: pDM589 was digested using PmeI to release *TIR1* for integration at *LEU2*. Next, pDM585 was used to generate *pKan-pCUP1-9xMyc-AID-stt4* for Stt4 N-terminal tagging by homologous recombination. Transformants were tested for auxin sensitivity and verified by PCR and DNA sequencing.

The *bem1 px* mutant (K338M, K348A, R349A, & R369A) was generated by directed mutagenesis of pDM256. The *bem1 px* coding sequence was then amplified by PCR and transformed into a *bem1Δ::CaURA3* strain (DMY2179). Transformants were selected for loss of the *URA3* marker on 5-FOA and integration of the *bem1 px* mutant was verified by PCR and sequencing, yielding DMY2199.

BEM1, *bem1 bc-14E,* and *bem1 bc-14E px* strains were generated using the pop-in-pop-out strategy (Sherman *et al*, 1974). In the first pop-in step, pDM865, pDM906, and pDM947 were linearized by digestion with an enzyme recognizing a restriction site within the *BEM1* or *bem1* ORF, then transformed into DMY2105 and selected on SC-URA for recombination at the *BEM1* locus. In the pop-out step, homologous recombination between the wild-type *BEM1* and juxtaposed *bem1* mutant occurs randomly, generating some transformants in which the wild-type or mutant *bem1* sequence is present at the *BEM1* locus. After counter selection against *URA3* on 5FOA media, transformants containing untagged *BEM1* or *bem1* at the genomic locus were identified by PCR and DNA sequencing.

The *cdc24 K513A-3xHA* mutant was generated by directed mutagenesis of pDM032, generating pDM737. The wild-type or mutant *cdc24 K513A-3xHA* was then integrated at the endogenous *CDC24* locus and checked by PCR, sequencing, and Western blotting using anti-HA antibodies.

Table EV2 contains a list of the yeast strains used in this study.

Protein expression and purification

GST-Bem1, Cdc24-6xHis, and derivative mutants were expressed and purified from Bl21-CodonPlus (DE3) cells, essentially as previously described (Rapali *et al*, 2017). Briefly, cells were grown in terrific broth at 37°C until an $OD600_{nm}$ ~3. Expression was induced by the addition of IPTG to 0.3 mM for Bem1 and 0.8 mM for Cdc24, after which cells were grown overnight at 18°C. Cells were then harvested and flash frozen in liquid nitrogen. The cell pellets were subsequently ground to a fine powder in a chilled coffee grinder.

For purification of Cdc24-6xHis, room temperature lysis buffer (50 mM Tris–Hcl (pH = 8.0), 1 M NaCl, 5 mM imidazole, 5% glycerol, 0.1% Tween) supplemented with EDTA-free protease inhibitor cocktail (Roche, Basel, Switzerland) and 1 mM freshly prepared PMSF was added to the chilled bacterial powder. After sonication on ice, the lysate was centrifuged at 70,000× *g* for 1 h and the supernatant was loaded on a Ni^{2+}-IMAC column. Beads were washed with 50 mM Tris–Hcl (pH = 8.0), 1 M NaCl, 20 mM imidazole, 5% glycerol, and 0.1% Tween, and Cdc24-6xHis was eluted with 20 mM

Tris–Hcl (pH = 8.0), 300 mM NaCl, and 500 mM imidazole. Cdc24-6xHis was extensively dialyzed (50 mM Tris–Hcl (pH = 8.0), 150 mM NaCl) then flash frozen in liquid nitrogen for storage. The same protocol was used to purify bem1 BCs-6xHis, except that the lysis buffer was modified (50 mM Tris–Hcl (pH = 7.5), 1 M NaCl, 5 mM imidazole, 5% glycerol, 0.5% Tween). The protein was analyzed on a 16% Tris-tricine gel (Schagger, 2006).

For GST-Bem1 purification, a modified lysis buffer was used [50 mM Tris–Hcl (pH = 7.5), 1 M NaCl, 0.1% Tween-20 and 5 mM DTT, EDTA-free protease inhibitor cocktail and 1 mM freshly prepared PMSF]. The lysate was sonicated, centrifuged as above, and the supernatant was added to glutathione agarose beads for 2 h in batch. After extensive washing (50 mM Tris–Hcl (pH = 7.5), 250 mM KCl, 0.05% Tween-20 and 0.5 mM DTT), the beads were equilibrated in 3C protease buffer (50 mM Hepes (pH = 7.6), 250 mM KCl, 0.05% Tween-20, and 0.5 mM DTT). The GST tag was digested directly on the glutathione agarose using the same buffer, supplemented with rhinovirus 3C protease. The flow-through, containing untagged Bem1, was dialyzed extensively in 50 mM Tris–Hcl (pH = 7.5), 150 mM NaCl then flash frozen in liquid nitrogen for storage.

Cdc42 lacking the C-terminal CAAX sequence was tagged with 10xHis and expressed and purified from Bl21-CodonPlus (DE3) cells. Room temperature lysis buffer (50 mM Tris–Hcl (pH = 7.5), 1 M NaCl, 25 mM imidazole), supplemented with EDTA-free protease inhibitor cocktail (Roche, Basel, Switzerland) and 1 mM freshly prepared PMSF, was added to bacterial powder. The lysate was stirred, sonicated, and centrifuged as described above, and the supernatant was loaded onto a Ni^{2+}-IMAC column. The column was washed in 50 mM Tris–Hcl (pH = 7.5), 1 M NaCl, and 25 mM imidazole, and Cdc42-10xHis was eluted in 20 mM Tris–Hcl (pH = 7.5), 300 mM NaCl, and 250 mM imidazole. To obtain nucleotide-free Cdc42, the protein was dialyzed in 20 mM Tris–Hcl (pH = 7.5), 150 mM NaCl, 5% glycerol supplemented with 25 mM EDTA, then dialyzed extensively [20 mM Tris–Hcl (pH = 7.5), 150 mM NaCl, 5% glycerol]. Samples were flash frozen in liquid nitrogen for storage.

Liposome preparation

Liposomes were prepared freshly from lipid stocks (Avanti Polar Lipids Inc., Alabaster, USA). The origin and composition of the lipids are provided in Table EV3. Lipids dissolved in chloroform were lyophilized for 15 min at 45°C to evaporate the chloroform. Lipids were washed in 50 µl ultrapure water and lyophilized until dry. Lipids were then resuspended in 20 mM Tris (pH = 7.5), 150 mM NaCl to have a final lipid concentration of 2 mM. After six cycles of freeze–thaw in liquid nitrogen and at 45°C in a water bath, liposomes were sonicated for 15 min in a bath sonicator. This method yielded monodisperse preparations of ~100 nm diameter liposomes, as assessed by dynamic light scattering.

Liposome floatation assays

The final concentration of liposomes was 0.5 mM in floatation experiments, while protein was 2 µM unless indicated differently. Liposomes were mixed with buffer alone [20 mM Tris (pH = 7.5), 150 mM NaCl], or with protein, in a final volume of 150 µl in a 500 µl polycarbonate ultracentrifuge tube. The mixtures were incubated at room temperature for 30 min. 100 µl of a 75% sucrose solution was mixed with the protein–liposome mixture to give a final sucrose concentration of 30%, which was gently overlaid with 200 µl of 25% sucrose. Finally, 50 µl of 20 mM Tris (pH = 7.5) and 150 mM NaCl was overlaid to give a final volume of 500 µl. Tubes were centrifuged for 1 h at 23°C at 120,000× *g*. 100 µl of supernatant and 200 µl of pellet were precipitated in 10% trichloroacetic acid. The pellet was resuspended in 15 µl of SDS–PAGE sample buffer [65 mM Tris–Hcl (pH = 6.8), 2% SDS, 10% glycerol, 5% β-mercapto ethanol, 100 mM β-glycerophosphate, 50 mM sodium fluoride], boiled for 5 min, analyzed by SDS–PAGE, and stained with Coomassie brilliant blue R250. The intensity of the protein bands in the supernatant and pellet was analyzed using a Bio-Rad Gel Doc system running Image Lab software.

The percentage of floating protein was calculated using the equation: $\{Supernatant^{band\ intensity}/(Supernatant^{band\ intensity} + Pellet^{band\ intensity})\} * 100$

Solid-state NMR spectroscopy

Liposomes containing POPC-d31, POPS, yeast extract lipids, ergosterol, brain $PI(4,5)P_2$, and brain PI(4)P were prepared by mixing appropriate powders depending on the liposomes composition in organic solvent (chloroform/methanol, 2:1) in the presence or absence of the Bem1 BC motifs (amino acids 1–72) and adjusting the lipid/protein ratio (25:1). Solvent was evaporated under a flow of N_2 to obtain a thin lipid film. Lipids were rehydrated with ultrapure water before lyophilization. The lipid powder was hydrated with an appropriate amount of buffer to give 50 mM Tris, 100 mM NaCl in deuterium-depleted water (80% hydration ratio), and homogenized by three cycles of vortexing, freezing (liquid nitrogen, −196°C, 1 min), and thawing (40°C in a water bath, 10 min). This protocol generated a milky suspension of micrometer-sized multilamellar vesicles. The molar composition of lipids used in NMR experiments is provided in Table EV4.

^2H NMR spectroscopy experiments were performed using a Bruker Avance II 500 MHz WB (11.75 T) spectrometer. ^2H NMR spectroscopy experiments on ^2H-labeled DMPC were performed at 76 MHz with a phase-cycled quadrupolar echo pulse sequence (90°x-t-90°y-t-acq). Acquisition parameters were as follows: spectral window of 500 kHz for ^2H NMR spectroscopy, p/2 pulse width of 3.90 ms for ^2H, interpulse delays (t) were of 40 ms, recycled delays of 2 s for ^2H; 3,000 scans were used for ^2H NMR spectroscopy. Spectra were processed using a Lorentzian line broadening of 300 Hz for ^2H NMR spectra before Fourier transformation from the top of the echo. Samples were equilibrated for 30 min at a given temperature before data acquisition. All spectra were processed and analyzed using Bruker Topspin 3.2 software. Spectral moments were calculated for each temperature using the NMR Depaker 1.0rc1 software [Copyright (C) 2009 Sébastien Buchoux]. Orientational order parameters (S_{CD}) were calculated from experimental quadrupolar splittings (Dn_Q) after spectra simulations according to equation 1:

$$\Delta\upsilon_Q(\theta) = \frac{3}{2}A_Q\left(\frac{3\cos^2\theta - 1}{2}\right)S_{CD} \quad (1)$$

in which A_Q, the quadrupolar coupling constant for methyl moieties, is 167 kHz, and q is the angle between the magnetic field and the bilayer normal.

Western blotting

Samples for Western blotting were prepared by collecting 1 $OD600_{nm}$ of mid-logarithmic phase cells, adding glass beads and flash freezing in liquid nitrogen (McCusker *et al*, 2007). Samples were vigorously agitated in 60 μl SDS sample buffer supplemented with 1 mM fresh PMSF. Samples were immediately boiled and analyzed by SDS–PAGE, Western blotting, and probed with appropriate antibodies.

Imaging

Cells were imaged using a widefield inverted microscope (Zeiss Axiovert 200M) with a 100× objective (oil, numerical aperture [NA] 1.4, plan Apo), and an electron-multiplying charge-coupled device (EMCCD) camera (Evolve; Photometrics, Tucson, AZ). MetaMorph 7.7 software (Molecular Devices, Sunnyvale, CA) was used for image acquisition and analysis. Filter sets LF488-B-000 (FFO2-482/18, FFO1-525/45, Di01-R488 [exciter, emitter, dichroic]) and LF561-A-000 (FFO2-561/14, FFO1-609/54, Di01-R561) were used to sequentially image cells expressing Bem1-GFP and Cdc24-mCherry (Jose *et al*, 2013).

Image analysis

Deconvolution was performed for visualization, where indicated, using a plug-in running within MetaMorph software (Jose *et al*, 2015). All Images were analyzed and processed using ImageJ software on raw data, not on deconvolved images.

To calculate the enrichment of PI4P at the plasma membrane, the integrated intensity (II) and area (A) of the entire cell (E) and the cytosol (C) were determined for each cell after background subtraction. Next, the mean gray value of the plasma membrane (MGVP) for each cell was determined as follows: MGVP = (IIE-IIC)/(AE-AC)). The values were plotted using GraphPad Prism software.

To calculate the enrichment of Bem1 at the pole, the mean gray value of the pole (MGVP) and the cell (MGVC) was determined for each cell using an empirically determined threshold value that enabled the cell pole to be identified. Next, the MGVP was normalized as follows: normalized mean gray value of the pole = (MGVP-MGVC)/MGVC). The values were plotted using GraphPad Prism software.

The same method was used to calculate the plasma membrane PI4P levels as a ratio between the pole (P) and the remainder of the cell (C). The mean gray value (MGV) of both was compared to obtain the ratio, R, using the formula: R = MGV P/MGV C.

Cdc24 GEF assay

Förster resonance energy transfer (FRET) between Cdc42 and N-methylanthraniloyl-GTP (mant-GTP) was measured to monitor the Cdc24-mediated GDP to mant-GTP exchange reaction on Cdc42 in real time. Trp97 of Cdc42, which is in close proximity to the GTP binding site, was excited using 280 nm wavelength light using a 5 nm bandwidth. The FRET signal was detected at the emission peak of mant-GTP, at 440 nm using an 8 nm bandwidth. All fluorescence measurements were performed at 27°C on a Tecan Infinite M1000PRO plate reader (Tecan Group, Männedorf, Germany) in 384-well, non-binding microplates (Greiner Bio-One, Courtaboeuf, France), in a 10 μl reaction volume. The final buffer conditions were 20 mM Tris–HCl (pH = 8.0), 150 mM NaCl, 1 mM DTT, 5 mM $MgCl_2$, 100 nM mant-GTP, supplemented with 100 μM GMP-PNP nucleotide. Cdc24 was used at a final concentration of 60 nM after 30 min room temperature pre-incubation with Bem1 at 5 μM. The reaction was initiated by adding Cdc42 to 9 μM final concentration and exchange was monitored for at least 2,000 s with 15 s intervals. For each sample, a mock reaction was used in the absence of GDP-loaded Cdc42 to normalize for bleaching and to subtract possible sources of background noise such as Cdc24-mant-GTP interaction. The intrinsic GDP to mant-GTP exchange rate of Cdc42 was determined in the absence of Cdc24.

Fitting of the kinetic trace data was performed in GraphPad Prism using a single exponential equation, and the observed kinetic rate constants were compared.

$$I = I_{Max} + (I_{Max} - I_{Min})(1 - e^{-k}obs^{t}),$$

Where I is the fluorescence intensity change, IMax is the maximal fluorescence intensity, IMin is the minimal fluorescence intensity, kobs is the observed kinetic rate constant, and t is the time in seconds.

Cdc24 affinity for anionic lipids in the presence of Bem1

The affinity of Cdc24 for anionic lipids in the presence of Bem1 was estimated using nonlinear regression analysis (Amezcua *et al*, 2002). In the analysis, we assume an approximate initial K_d between Cdc24 and anionic lipids of 1 μM (Yu *et al*, 2004). A nonlinear regression fit with equation 2 was used to obtain the corresponding K_d for the Cdc24 interaction with anionic lipids in the presence of Bem1:

$$\begin{aligned} Y = {} & Nu + (Nb - Nu) * \{(x + (P) + K_d) - [(x + (P) + K_d)^2 \\ & - (4 * x * (P))]^{0.5}\}/(2 * (P)) \end{aligned} \quad (2)$$

where Y is the percentage of Cdc24 found in the supernatant at the lipid concentration P. P was chosen based on the following: First, around 30% of Cdc24 interacted with anionic liposomes (see Fig 5B). Second, the PH domain is assumed to interact with 3–5 lipid molecules (Ni *et al*, 2017). In the floatation experiments involving Bem1 and Cdc24 shown in Fig 5B–D, 1 μM of Cdc24 was used, so P = [Cdc24]*(30%)*3 lipid molecules = 0.9 μM lipids that are estimated to interact with Cdc24. In the equation, Nu and Nb are the maximum unbound and bound percentage of Cdc24, respectively, and x is the Bem1 concentration.

Single-particle tracking photoactivation localization microscopy (sptPALM)

Live cells were imaged using a widefield, inverted microscope (Axiovert 200M; Carl Zeiss, Marly le Roi, France) equipped with a 100× TIRFM objective (oil, NA 1.46, plan Apo), iLas^2 TIRF system (Roper Scientific), and an EMCCD camera (Evolve; Photometrics, Tuscon, Arizona). The imaging system was maintained at a constant

temperature of 25°C using a custom designed incubator (Box and Cube, Life Imaging System, Basel, Switzerland). MetaMorph 7.7 software (Molecular Devices, Sunnyvale, USA) was used for image acquisition and analysis.

For *in vivo* imaging, cells expressing mEOS-Cdc42 were grown to mid-log phase and imaged at 25°C. Coverslips (High precision 18 × 18 mm, 1.5 H, Marienfeld, Lauda-Königshofen, Germany) were washed overnight in a solution of 1M Hcl and 1M HNO_3 then rinsed three times the next day in ultrapure water. After a 30-min incubation in water, then 30 min in ethanol, the coverslips were dried and used for imaging. Imaging was performed in a highly oblique illumination (HiLo) mode. mEOS-Cdc42 cells were imaged using a 561-nm laser with additional continuous photoconversion using a 405-nm laser. The 405-nm laser was maintained at low power (0.3–1 μW) for adequate separation of stochastically converted molecules. The iLas^2 system was used in arc mode for live imaging and ellipse mode for fixed samples. These settings set the pattern of rotation of the lasers on the back focal plane of the TIRF objective. The fluorescence was collected on the EMCCD camera after passing through a combination of dichroic and emission filters (D101-R561 and F39-617, respectively; Chroma, Bellows Falls, VT). Images were acquired in streaming mode at 50 Hz (20 ms exposure time). During *in vivo* imaging, 16,000–20,000 images were collected for each cell. Multicolor fluorescent 100 nm beads (Tetraspeck, Invitrogen) were used as fiduciary markers in all super-resolution imaging experiments to register long-term acquisitions for lateral drift correction.

For fixed-cell imaging, cells were grown to log phase ($OD_{600\ nm}$ of < 0.8) and fixed with 3.7% formaldehyde and 0.2% glutaraldehyde for 10 min. After washing in PBS three times, cells were resuspended in PBS and directly used for imaging. Image acquisition of fixed cells was performed using the same protocol as for living cells, as described above. 32,000–40,000 images were acquired per cell, at which point the pool of photoconvertible single molecules was completely depleted.

Single-particle localization, tracking, and nanocluster detection by Voronoï Tessellation

Image stacks collected for each sptPALM experiment were analyzed using a custom-written software operating as a plug-in within MetaMorph software, PalmTracer, to compute single-molecule localizations and dynamics. Single molecules were localized in each image frame and tracked over time using wavelet segmentation and simulated annealing algorithms (Sartorel *et al*, 2018). The sptPALM image resolution, defined as FWHM = 2.3 × the pointing accuracy, was estimated to 48 nm. The pointing accuracy, measured to be 20.86 nm, was computed from the acquisition of mEOS-Cdc42 in fixed cells by bidimensional Gaussian fitting of the spatial distribution of 80 single molecules localized for more than 20 consecutive time points. Tracking data and subsequent MSDs were generated from the membrane-bound population of mEOS-Cdc42. Proteins in the freely diffusing cytosolic pool of mEOS-Cdc42 were not tracked in these experiments because cytosolic diffusion is much higher than diffusion in a membrane environment, and would not be localized and tracked with 20 ms exposure time.

In our observations, all MSDs have a quasi-linear dependence at short times, enabling computation of the instantaneous diffusion coefficient (D) per molecule by linear regression on the first four points of the MSD of all trajectories that are longer than six consecutive frames.

Cdc42 nanoclusters were quantified from the reconstructed super-resolution images of fixed cells using SR-Tesseler analysis (Sartorel *et al*, 2018). This software is based on Voronoï tessellation, wherein single-molecule localizations are treated as seeds around which polygons are assembled. In our analysis, we defined regions of interest (ROI) as the pole or non-pole of the cell after visual inspection of the widefield 491 nm image acquired at the outset of the experiment. The surface area of the polygon drawn around the detected single molecule is proportional to the local molecular density, such that the area of the polygon decreases as the local density of single-molecule localizations increases. PALM images were corrected for single-molecule blinking within the SR-Tesseler software (Sartorel *et al*, 2018). This takes into account mEOS photophysics, and a pointing accuracy of 20 nm as a radius of search, which would otherwise overestimate the number of single-molecule detections. After blinking correction, nanoclusters were defined as those areas containing a minimum of five localizations at a local density that was at least twofold higher than the average density within the selected ROI. Nanocluster characteristics including diameter, area, and the number of localizations were exported from SR-Tesseler into Excel (Microsoft) for further statistical analysis.

Statistical analysis

The diffusion coefficients were represented as box plots displaying the median as a line and the percentiles (25–75%). Statistical comparisons were made using a non-parametric, two-tailed Mann–Whitney rank sum test. Non-Gaussian distributions of nanocluster sizes were represented by data-points displaying median as a line and the percentiles (25–75%) and also compared using a non-parametric, two-tailed Mann–Whitney rank sum test. Statistical analyses were based on cluster area values calculated by SR-Tesseler. Only areas > 2,000 nm^2 were used, corresponding to a diameter of 48 nm, the resolution of our imaging system.

Expanded View for this article is available online.

Acknowledgements

We thank Cameron Mackereth for advice on nonlinear regression analysis and Jean-Baptiste Sibarita for providing PALM imaging analysis software. We also thank Bertrand Daignan-Fornier for anti-Ade13 antibody, Helle Ulrich and Douglas Koshland for AID/TIR plasmids, and Nelly Savarit, Melanie Sevrin, and Laure Bataille for performing preliminary liposome floatation experiments. Anne Royou and Andrew Weatherall are acknowledged for their continued support. We thank Jean-Louis Mergny for the use of his fluorescence plate reader. This work received funding from the University of Bordeaux through the Synthetic Biology in Bordeaux (SB2) Program and a Doctoral School Fellowship to JM. This work was also funded by the CNRS through the Interdisciplinary Research Initiative, Agence Nationale de la Recherche (ANR) through Program Blanc grant ANR-13-BSV2-0015-01 and ANR-14-CE09-0020-01, the Regional Council of Aquitaine, the European Research Council (ERC-2015-StG GA no. 639020 to A.L.) and the IdEx Bordeaux (Chaire d'Installation to

B.H., ANR-10-IDEX-03-02). This project received funding from the European Union's Horizon 2020 research and innovation program under the Marie Sklodowska-Curie Grant agreement no. 708972—"Lipids and Polarity".

Author contributions

DMc conceived the study. All authors designed experiments and analyzed the data. JM, AML, and ES performed the experiments, with the exception of NMR spectroscopy, which was performed by DMa and analyzed by AL and BH. DMc wrote the manuscript with input from the co-authors.

Conflict of interest

The authors declare that they have no conflict of interest.

References

Amezcua CA, Harper SM, Rutter J, Gardner KH (2002) Structure and interactions of PAS kinase N-terminal PAS domain: model for intramolecular kinase regulation. *Structure* 10: 1349 – 1361

Atkinson K, Fogel S, Henry SA (1980) Yeast mutant defective in phosphatidylserine synthesis. *J Biol Chem* 255: 6653 – 6661

Atwood SX, Chabu C, Penkert RR, Doe CQ, Prehoda KE (2007) Cdc42 acts downstream of Bazooka to regulate neuroblast polarity through Par-6 aPKC. *J Cell Sci* 120: 3200 – 3206

Bailey MJ, Prehoda KE (2015) Establishment of par-polarized cortical domains via phosphoregulated membrane motifs. *Dev Cell* 35: 199 – 210

Bender A, Pringle JR (1991) Use of a screen for synthetic lethal and multicopy suppressee mutants to identify two new genes involved in morphogenesis in *Saccharomyces cerevisiae*. *Mol Cell Biol* 11: 1295 – 1305

Bender L, Lo HS, Lee H, Kokojan V, Peterson V, Bender A (1996) Associations among PH and SH3 domain-containing proteins and Rho-type GTPases in yeast. *J Cell Biol* 133: 879 – 894

Bose I, Irazoqui JE, Moskow JJ, Bardes ES, Zyla TR, Lew DJ (2001) Assembly of scaffold-mediated complexes containing Cdc42p, the exchange factor Cdc24p, and the effector Cla4p required for cell cycle-regulated phosphorylation of Cdc24p. *J Biol Chem* 276: 7176 – 7186

Buchkovich NJ, Henne WM, Tang S, Emr SD (2013) Essential N-terminal insertion motif anchors the ESCRT-III filament during MVB vesicle formation. *Dev Cell* 27: 201 – 214

Butty AC, Perrinjaquet N, Petit A, Jaquenoud M, Segall JE, Hofmann K, Zwahlen C, Peter M (2002) A positive feedback loop stabilizes the guanine-nucleotide exchange factor Cdc24 at sites of polarization. *EMBO J* 21: 1565 – 1576

Chant J, Corrado K, Pringle JR, Herskowitz I (1991) Yeast BUD5, encoding a putative GDP-GTP exchange factor, is necessary for bud site selection and interacts with bud formation gene BEM1. *Cell* 65: 1213 – 1224

Chung J, Torta F, Masai K, Lucast L, Czapla H, Tanner LB, Narayanaswamy P, Wenk MR, Nakatsu F, De Camilli P (2015) Intracellular transport. PI4P/phosphatidylserine countertransport at ORP5- and ORP8-mediated ER-plasma membrane contacts. *Science* 349: 428 – 432

Das A, Slaughter BD, Unruh JR, Bradford WD, Alexander R, Rubinstein B, Li R (2012) Flippase-mediated phospholipid asymmetry promotes fast Cdc42 recycling in dynamic maintenance of cell polarity. *Nat Cell Biol* 14: 304 – 310

Das S, Yin T, Yang Q, Zhang J, Wu YI, Yu J (2015) Single-molecule tracking of small GTPase Rac1 uncovers spatial regulation of membrane translocation and mechanism for polarized signaling. *Proc Natl Acad Sci USA* 112: E267 – E276

Drubin DG, Nelson WJ (1996) Origins of cell polarity. *Cell* 84: 335 – 344

Fairn GD, Hermansson M, Somerharju P, Grinstein S (2011) Phosphatidylserine is polarized and required for proper Cdc42 localization and for development of cell polarity. *Nat Cell Biol* 13: 1424 – 1430

Finegold AA, Johnson DI, Farnsworth CC, Gelb MH, Judd SR, Glomset JA, Tamanoi F (1991) Protein geranylgeranyl transferase of *Saccharomyces cerevisiae* is specific for Cys-Xaa-Xaa-Leu motif proteins and requires the *CDC43* gene product but not the *DPR1* gene product. *Proc Natl Acad Sci USA* 88: 4448 – 4452

Fletcher GC, Lucas EP, Brain R, Tournier A, Thompson BJ (2012) Positive feedback and mutual antagonism combine to polarize Crumbs in the *Drosophila* follicle cell epithelium. *Curr Biol* 22: 1116 – 1122

Ghomashchi F, Zhang X, Liu L, Gelb MH (1995) Binding of prenylated and polybasic peptides to membranes: affinities and intervesicle exchange. *Biochemistry* 34: 11910 – 11918

Goryachev AB, Pokhilko AV (2008) Dynamics of Cdc42 network embodies a turing-type mechanism of yeast cell polarity. *FEBS Lett* 582: 1437 – 1443

Gotta M, Abraham MC, Ahringer J (2001) CDC-42 controls early cell polarity and spindle orientation in *C. elegans*. *Curr Biol* 11: 482 – 488

Gronnier J, Crowet JM, Habenstein B, Nasir MN, Bayle V, Hosy E, Platre MP, Gouguet P, Raffaele S, Martinez D, Grelard A, Loquet A, Simon-Plas F, Gerbeau-Pissot P, Der C, Bayer EM, Jaillais Y, Deleu M, Germain V, Lins L *et al* (2017) Structural basis for plant plasma membrane protein dynamics and organization into functional nanodomains. *Elife* 6: e26404

Grossmann G, Opekarova M, Malinsky J, Weig-Meckl I, Tanner W (2007) Membrane potential governs lateral segregation of plasma membrane proteins and lipids in yeast. *EMBO J* 26: 1 – 8

Gulli MP, Jaquenoud M, Shimada Y, Niederhauser G, Wiget P, Peter M (2000) Phosphorylation of the Cdc42 exchange factor Cdc24 by the PAK-like kinase Cla4 may regulate polarized growth in yeast. *Mol Cell* 6: 1155 – 1167

Haupt A, Minc N (2017) Gradients of phosphatidylserine contribute to plasma membrane charge localization and cell polarity in fission yeast. *Mol Biol Cell* 28: 210 – 220

Hayakawa A, Hayes SJ, Lawe DC, Sudharshan E, Tuft R, Fogarty K, Lambright D, Corvera S (2004) Structural basis for endosomal targeting by FYVE domains. *J Biol Chem* 279: 5958 – 5966

Hokanson DE, Laakso JM, Lin T, Sept D, Ostap EM (2006) Myo1c binds phosphoinositides through a putative pleckstrin homology domain. *Mol Biol Cell* 17: 4856 – 4865

Irazoqui JE, Gladfelter AS, Lew DJ (2003) Scaffold-mediated symmetry breaking by Cdc42p. *Nat Cell Biol* 5: 1062 – 1070

Ito T, Matsui Y, Ago T, Ota K, Sumimoto H (2001) Novel modular domain PB1 recognizes PC motif to mediate functional protein-protein interactions. *EMBO J* 20: 3938 – 3946

Janke C, Magiera MM, Rathfelder N, Taxis C, Reber S, Maekawa H, Moreno-Borchart A, Doenges G, Schwob E, Schiebel E, Knop M (2004) A versatile toolbox for PCR-based tagging of yeast genes: new fluorescent proteins, more markers and promoter substitution cassettes. *Yeast* 21: 947 – 962

Johnson DI, Pringle JR (1990) Molecular characterization of CDC42, a *Saccharomyces cerevisiae* gene involved in the development of cell polarity. *J Cell Biol* 111: 143 – 152

Jose M, Tollis S, Nair D, Sibarita JB, McCusker D (2013) Robust polarity establishment occurs via an endocytosis-based cortical corralling mechanism. *J Cell Biol* 200: 407 – 418

Jose M, Tollis S, Nair D, Mitteau R, Velours C, Massoni-Laporte A, Royou A, Sibarita JB, McCusker D (2015) A quantitative imaging-based screen

reveals the exocyst as a network hub connecting endo- and exocytosis. *Mol Biol Cell* 26: 2519 – 2534

Kay AJ, Hunter CP (2001) CDC-42 regulates PAR protein localization and function to control cellular and embryonic polarity in *C. elegans*. *Curr Biol* 11: 474 – 481

Kelly RC, Jensen DE, von Hippel PH (1976) DNA "melting" proteins. IV. Fluorescence measurements of binding parameters for bacteriophage T4 gene 32-protein to mono-, oligo-, and polynucleotides. *J Biol Chem* 251: 7240 – 7250

Kozminski KG, Chen AJ, Rodal AA, Drubin DG (2000) Functions and functional domains of the GTPase Cdc42p. *Mol Biol Cell* 11: 339 – 354

Lemmon MA, Ferguson KM (2000) Signal-dependent membrane targeting by pleckstrin homology (PH) domains. *Biochem J* 350(Pt 1): 1 – 18

Longtine MS, McKenzie A, DeMarini D, Shah NG, Wach A, Brachat A, Philippsen P, Pringle JR (1998) Additional modules for versatile and economical PCR-based gene deletion and modification in *Saccharomyces cerevisiae*. *Yeast* 14: 953 – 961

McCusker D, Denison C, Anderson S, Egelhofer TA, Yates JR III, Gygi SP, Kellogg DR (2007) Cdk1 coordinates cell-surface growth with the cell cycle. *Nat Cell Biol* 9: 506 – 515

Morawska M, Ulrich HD (2013) An expanded tool kit for the auxin-inducible degron system in budding yeast. *Yeast* 30: 341 – 351

Moser von Filseck J, Copic A, Delfosse V, Vanni S, Jackson CL, Bourguet W, Drin G (2015) Intracellular transport. Phosphatidylserine transport by ORP/Osh proteins is driven by phosphatidylinositol 4-phosphate. *Science* 349: 432 – 436

Murakoshi H, Iino R, Kobayashi T, Fujiwara T, Ohshima C, Yoshimura A, Kusumi A (2004) Single-molecule imaging analysis of Ras activation in living cells. *Proc Natl Acad Sci USA* 101: 7317 – 7322

Nan X, Tamguney TM, Collisson EA, Lin LJ, Pitt C, Galeas J, Lewis S, Gray JW, McCormick F, Chu S (2015) Ras-GTP dimers activate the mitogen-activated protein kinase (MAPK) pathway. *Proc Natl Acad Sci USA* 112: 7996 – 8001

Ni T, Kalli AC, Naughton FB, Yates LA, Naneh O, Kozorog M, Anderluh G, Sansom MS, Gilbert RJ (2017) Structure and lipid-binding properties of the kindlin-3 pleckstrin homology domain. *Biochem J* 474: 539 – 556

Nishimura K, Fukagawa T, Takisawa H, Kakimoto T, Kanemaki M (2009) An auxin-based degron system for the rapid depletion of proteins in nonplant cells. *Nat Methods* 6: 917 – 922

Papayannopoulos V, Co C, Prehoda KE, Snapper S, Taunton J, Lim WA (2005) A polybasic motif allows N-WASP to act as a sensor of PIP(2) density. *Mol Cell* 17: 181 – 191

Peterson J, Zheng Y, Bender L, Myers L, Cerione R, Bender A (1994) Interactions between the bud emergence proteins Bem1p and Bem2p and Rho-type GTPases in yeast. *J Cell Biol* 127: 1395 – 1406

Raghupathy R, Anilkumar AA, Polley A, Singh PP, Yadav M, Johnson C, Suryawanshi S, Saikam V, Sawant SD, Panda A, Guo Z, Vishwakarma RA, Rao M, Mayor S (2015) Transbilayer lipid interactions mediate nanoclustering of lipid-anchored proteins. *Cell* 161: 581 – 594

Rapali P, Mitteau R, Braun C, Massoni-Laporte A, Unlu C, Bataille L, Arramon FS, Gygi SP, McCusker D (2017) Scaffold-mediated gating of Cdc42 signalling flux. *Elife* 6: e25257

Remorino A, De Beco S, Cayrac F, Di Federico F, Cornilleau G, Gautreau A, Parrini MC, Masson JB, Dahan M, Coppey M (2017) Gradients of Rac1 nanoclusters support spatial patterns of Rac1 signaling. *Cell Rep* 21: 1922 – 1935

Richman TJ, Sawyer MM, Johnson DI (2002) *Saccharomyces cerevisiae* Cdc42p localizes to cellular membranes and clusters at sites of polarized growth. *Eukaryot Cell* 1: 458 – 468

Richman TJ, Toenjes KA, Morales SE, Cole KC, Wasserman BT, Taylor CM, Koster JA, Whelihan MF, Johnson DI (2004) Analysis of cell-cycle specific localization of the Rdi1p RhoGDI and the structural determinants required for Cdc42p membrane localization and clustering at sites of polarized growth. *Curr Genet* 45: 339 – 349

Sartorel E, Unlu C, Jose M, Massoni-Laporte A, Meca J, Sibarita JB, McCusker D (2018) Phosphatidylserine and GTPase activation control Cdc42 nanoclustering to counter dissipative diffusion. *Mol Biol Cell* 29: 1299 – 1310

Schagger H (2006) Tricine-SDS-PAGE. *Nat Protoc* 1: 16 – 22

Schink KO, Tan KW, Stenmark H (2016) Phosphoinositides in control of membrane dynamics. *Annu Rev Cell Dev Biol* 32: 143 – 171

Sciorra VA, Audhya A, Parsons AB, Segev N, Boone C, Emr SD (2005) Synthetic genetic array analysis of the PtdIns 4-kinase Pik1p identifies components in a Golgi-specific Ypt31/rab-GTPase signaling pathway. *Mol Biol Cell* 16: 776 – 793

Seaman MN, Williams HP (2002) Identification of the functional domains of yeast sorting nexins Vps5p and Vps17p. *Mol Biol Cell* 13: 2826 – 2840

Sherman F, Fink G, Lawrence C (1974) *Methods in yeast genetics*. Cold Spring Harbor, NY: Cold Spring Harbor Laboratory Press

Slaughter BD, Unruh JR, Das A, Smith SE, Rubinstein B, Li R (2013) Non-uniform membrane diffusion enables steady-state cell polarization via vesicular trafficking. *Nat Commun* 4: 1380

Snaith HA, Sawin KE (2003) Fission yeast mod5p regulates polarized growth through anchoring of tea1p at cell tips. *Nature* 423: 647 – 651

Solanko LM, Sullivan DP, Sere YY, Szomek M, Lunding A, Solanko KA, Pizovic A, Stanchev LD, Pomorski TG, Menon AK, Wustner D (2018) Ergosterol is mainly located in the cytoplasmic leaflet of the yeast plasma membrane. *Traffic* 19: 198 – 214

Srinivasan S, Wang F, Glavas S, Ott A, Hofmann F, Aktories K, Kalman D, Bourne HR (2003) Rac and Cdc42 play distinct roles in regulating PI (3,4,5)P3 and polarity during neutrophil chemotaxis. *J Cell Biol* 160: 375 – 385

Stahelin RV, Karathanassis D, Murray D, Williams RL, Cho W (2007) Structural and membrane binding analysis of the Phox homology domain of Bem1p: basis of phosphatidylinositol 4-phosphate specificity. *J Biol Chem* 282: 25737 – 25747

Stefan CJ, Audhya A, Emr SD (2002) The yeast synaptojanin-like proteins control the cellular distribution of phosphatidylinositol (4,5)-bisphosphate. *Mol Biol Cell* 13: 542 – 557

Stowers L, Yelon D, Berg LJ, Chant J (1995) Regulation of the polarization of T cells toward antigen-presenting cells by Ras-related GTPase CDC42. *Proc Natl Acad Sci USA* 92: 5027 – 5031

Tian T, Harding A, Inder K, Plowman S, Parton RG, Hancock JF (2007) Plasma membrane nanoswitches generate high-fidelity Ras signal transduction. *Nat Cell Biol* 9: 905 – 914

Toenjes KA, Simpson D, Johnson DI (2004) Separate membrane targeting and anchoring domains function in the localization of the *S. cerevisiae* Cdc24p guanine nucleotide exchange factor. *Curr Genet* 45: 257 – 264

Wedlich-Soldner R, Wai SC, Schmidt T, Li R (2004) Robust cell polarity is a dynamic state established by coupling transport and GTPase signaling. *J Cell Biol* 166: 889 – 900

Weiner OD, Neilsen PO, Prestwich GD, Kirschner MW, Cantley LC, Bourne HR (2002) A PtdInsP(3)- and Rho GTPase-mediated positive feedback loop regulates neutrophil polarity. *Nat Cell Biol* 4: 509 – 513

Witte K, Strickland D, Glotzer M (2017) Cell cycle entry triggers a switch between two modes of Cdc42 activation during yeast polarization. *Elife* 6: e26722

Yakir-Tamang L, Gerst JE (2009) A phosphatidylinositol-transfer protein and phosphatidylinositol-4-phosphate 5-kinase control Cdc42 to regulate the actin cytoskeleton and secretory pathway in yeast. *Mol Biol Cell* 20: 3583 – 3597

Yamaguchi Y, Ota K, Ito T (2007) A novel Cdc42-interacting domain of the yeast polarity establishment protein Bem1. Implications for modulation of mating pheromone signaling. *J Biol Chem* 282: 29 – 38

Yeung T, Gilbert GE, Shi J, Silvius J, Kapus A, Grinstein S (2008) Membrane phosphatidylserine regulates surface charge and protein localization. *Science* 319: 210 – 213

Yu JW, Lemmon MA (2001) All phox homology (PX) domains from Saccharomyces cerevisiae specifically recognize phosphatidylinositol 3-phosphate. *J Biol Chem* 276: 44179 – 44184

Yu JW, Mendrola JM, Audhya A, Singh S, Keleti D, DeWald DB, Murray D, Emr SD, Lemmon MA (2004) Genome-wide analysis of membrane targeting by *S. cerevisiae* pleckstrin homology domains. *Mol Cell* 13: 677 – 688

Zhong S, Hsu F, Stefan CJ, Wu X, Patel A, Cosgrove MS, Mao Y (2012) Allosteric activation of the phosphoinositide phosphatase Sac1 by anionic phospholipids. *Biochemistry* 51: 3170 – 3177

Zhou Y, Wong CO, Cho KJ, van der Hoeven D, Liang H, Thakur DP, Luo J, Babic M, Zinsmaier KE, Zhu MX, Hu H, Venkatachalam K, Hancock JF (2015) Signal transduction. Membrane potential modulates plasma membrane phospholipid dynamics and K-Ras signaling. *Science* 349: 873 – 876

Zhou Y, Prakash P, Liang H, Cho KJ, Gorfe AA, Hancock JF (2017) Lipid-sorting specificity encoded in K-Ras membrane anchor regulates signal output. *Cell* 168: 239 – 251 e16